Chella, Federico; Marzetti, Laura; Stenroos, Matti; Parkkonen, Lauri; Ilmoniemi, Risto J.; Romani, Gian Luca; Pizzella, Vittorio

The impact of improved MEG–MRI co-registration on MEG connectivity analysis

Published in:
NeuroImage

DOI:
10.1016/j.neuroimage.2019.04.061

Published: 01/05/2019

Document Version
Publisher's PDF, also known as Version of record

NeuroImage 197 (2019) 354–367

Contents lists available at ScienceDirect

NeuroImage

journal homepage: www.elsevier.com/locate/neuroimage

The impact of improved MEG–MRI co-registration on MEG connectivity analysis

Federico Chella [a,b,*], Laura Marzetti [a,b], Matti Stenroos [c], Lauri Parkkonen [c], Risto J. Ilmoniemi [c], Gian Luca Romani [b], Vittorio Pizzella [a,b]

[a] Department of Neuroscience, Imaging and Clinical Sciences, G. d'Annunzio University of Chieti-Pescara, via dei Vestini 31, 66100 Chieti, Italy
[b] Institute for Advanced Biomedical Technologies, G. d'Annunzio University of Chieti-Pescara, via dei Vestini 31, 66100 Chieti, Italy
[c] Department of Neuroscience and Biomedical Engineering, Aalto University School of Science, P.O. Box 12200, FI, 00076, Aalto, Finland

ARTICLE INFO

Keywords:
MEG
Co-registration
Brain connectivity
Beamforming
Minimum-norm estimate
Volume-conductor modeling

ABSTRACT

Co-registration between structural head images and functional MEG data is needed for anatomically-informed MEG data analysis. Despite the efforts to minimize the co-registration error, conventional landmark- and surface-based strategies for co-registering head and MEG device coordinates achieve an accuracy of typically 5–10 mm. Recent advances in instrumentation and technical solutions, such as the development of hybrid ultra-low-field (ULF) MRI–MEG devices or the use of 3D-printed individualized foam head-casts, promise unprecedented co-registration accuracy, i.e., 2 mm or better. In the present study, we assess through simulations the impact of such an improved co-registration on MEG connectivity analysis.

We generated synthetic MEG recordings for pairs of connected cortical sources with variable locations. We then assessed the capability to reconstruct source-level connectivity from these recordings for 0–15-mm co-registration error, three levels of head modeling detail (one-, three- and four-compartment models), two source estimation techniques (linearly constrained minimum-variance beamforming and minimum-norm estimation MNE) and five separate connectivity metrics (imaginary coherency, phase-locking value, amplitude-envelope correlation, phase-slope index and frequency-domain Granger causality).

We found that beamforming can better take advantage of an accurate co-registration than MNE. Specifically, when the co-registration error was smaller than 3 mm, the relative error in connectivity estimates was down to one-third of that observed with typical co-registration errors. MNE provided stable results for a wide range of co-registration errors, while the performance of beamforming rapidly degraded as the co-registration error increased. Furthermore, we found that even moderate co-registration errors (>6 mm, on average) essentially decrease the difference of four- and three- or one-compartment models. Hence, a precise co-registration is important if one wants to take full advantage of highly accurate head models for connectivity analysis.

We conclude that an improved co-registration will be beneficial for reliable connectivity analysis and effective use of highly accurate head models in future MEG connectivity studies.

1. Introduction

Brain operation relies on the functional segregation and integration of several brain areas into networks (Avena-Koenigsberger et al., 2018). The functional relevance of cross-areal associations has been extensively demonstrated (see Cole et al., 2014 for a review). Most of these studies have used functional Magnetic Resonance Imaging (fMRI) to investigate the coupling of slow fluctuations in blood oxygenation during task execution and during inactivity, the latter leading to the concept of resting-state networks (Raichle, 2010).

To investigate cross-areal coupling at behaviorally relevant temporal scales, e.g., in the 10–100 ms range, fMRI is inadequate due to its intrinsic poor temporal resolution. Electrophysiological techniques, such as magnetoencephalography (MEG) or electroencephalography (EEG), offer a solution to this problem thanks to their exquisite temporal resolution (Baillet, 2017; Hämäläinen et al., 1993). In this framework, several

* Corresponding author. Department of Neuroscience, Imaging and Clinical Sciences, G. d'Annunzio University of Chieti-Pescara, via dei Vestini 31, 66100 Chieti, Italy.
E-mail address: federico.chella@unich.it (F. Chella).

https://doi.org/10.1016/j.neuroimage.2019.04.061
Received 9 July 2018; Received in revised form 13 April 2019; Accepted 23 April 2019
Available online 25 April 2019

strategies have been developed to detect functional associations, including investigations of the coupling of slow signal fluctuations, in analogy with the fMRI network approach (Brookes et al., 2011a; de Pasquale et al., 2010; Liu et al., 2017; O'Neill et al., 2015). Phase locking of oscillatory activity, i.e., of brain rhythms, is a plausible candidate mechanism behind cross-areal integration (Engel et al., 2013; Fries, 2015; Varela et al., 2001). Noninvasive access to neuronal oscillations is exclusively provided by MEG or EEG. Along this line, MEG has substantially contributed to unravelling the oscillatory coupling between cortical regions (e.g., Basti et al., 2018; Chella et al., 2016; D'Andrea et al., 2019; Lobier et al., 2018; Marzetti et al., 2013; Palva and Palva, 2012; Siegel et al., 2008).

The identification of neuronal generators from MEG signals requires one to solve an ill-posed inverse problem. Besides the intrinsic non-uniqueness and the properties of the techniques used to render the solution unique, the accuracy of the solution is limited by the knowledge of the conductivity geometry of the head (described as the head model) as well as of MEG sensor positions relative to the head; this knowledge, along with sensor type and geometry, determines the sensitivity distributions of the sensors, i.e., the lead field matrix. The accuracy of this information, in turn, affects the reliability and reproducibility of the estimates of cross-areal associations.

To date, realistically shaped and sufficiently detailed head models can be constructed from structural head images (usually MRI scans); several forward-modeling techniques have been developed to take into account the effect of relevant head tissues, such as the boundary-element method (BEM) (Hämäläinen and Sarvas, 1989; Mosher et al., 1999; Stenroos and Nummenmaa, 2016), and the finite-element method (Haueisen et al., 1997; Schimpf et al., 2002; Wolters et al., 2006, 2004). Including the cerebrospinal fluid (CSF) and the distinction between white and gray matter have in simulations been shown to improve the accuracy of MEG forward solutions (Stenroos and Nummenmaa, 2016; Vorwerk et al., 2014). Similar results have been obtained for inverse solutions involving one source at a time (Neugebauer et al., 2017) and for connectivity estimates (Cho et al., 2015). Nevertheless, when using structural images for modeling MEG, a precise co-registration between functional and anatomical data is required for accurate forward modeling.

In MEG recordings, co-registration errors are typically several millimeters. As an example, Whalen et al. (2008) reported a mean error of 8.7 mm for co-registration based on a small set of anatomical reference points, which can be reduced down to 4.4 mm by using surface-matching techniques. Adjamian et al. (2004) used personalized bite bars with extra fiducial coils, achieving a co-registration accuracy of about 5 mm. Hillebrand and Barnes (2011) suggested that a reasonable bound for co-registration error is between 5 and 10 mm. These findings suggest that co-registration errors can be quite large, and thus possible effects on source and connectivity estimation should be carefully taken into account when designing MEG experiments. Besides co-registration, subject movements within or across different MEG sessions represent a related source of error on the assumed head location relative to sensors. The magnitude of head movements is often greater than co-registration errors. As an example, Wehner et al. (2008) reported an average head displacement up to 12 mm from the beginning to the end of the experiment in a study with children. Head movements can be corrected for in software (Taulu and Simola, 2006; Uutela et al., 2001), but even in this case the remaining co-registration error represents the absolute limit for forward modeling accuracy, which cannot be further reduced.

Recent technical solutions and advances in instrumentation allow for improved MEG–MRI co-registration. Troebinger et al. (2014) proposed the use of subject-specific head casts produced with 3D printing technologies to constrain head movements within and between MEG sessions, reducing co-registration variability to be below 2 mm and the absolute co-registration error below 5 mm. Sonntag et al. (2018) reported an improved co-registration based on a Metropolis sampling algorithm, achieving an average uncertainty of about 1.7 mm on the head surface, with an upper bound of 4 mm. This is of the same order of magnitude as expected from novel instrumentation for biomagnetic measurements that combines ultra-low-field (ULF) MRI with MEG (Vesanen et al., 2013; Zotev et al., 2008), where no co-registration between MEG and ULF MRI is required (Mäkinen et al., 2019); one will only need to match ULF MRI with conventional high-field MRI to provide high-quality structural images (Guidotti et al., 2018).

Co-registration errors have been shown to degrade source reconstruction accuracy (Barratt et al., 2018; Hillebrand and Barnes, 2011, 2003; López et al., 2012; Zetter et al., 2018). Nonetheless, the effects of co-registration errors on source connectivity estimates have, to our knowledge, only been investigated for beamformer reconstruction by Liuzzi et al. (2017), who reported reduced reliability and reproducibility of functional connectivity estimates due to erroneous co-registration.

This study aims at a quantitative evaluation of the impact of co-registration errors on the estimation of functional brain connectivity, taking also into account head-model accuracy and the source-reconstruction technique. We approach these aims through extensive simulations in which synthetic MEG recordings with known connectivity patterns are considered. We use three levels of detail in volume-conductor test models, namely the four-, three- and one-compartment models, and two source-reconstruction techniques, namely minimum-norm estimation (Hämäläinen and Ilmoniemi, 1994; Lin et al., 2004) and beamforming (van Veen et al., 1997). We consider five conventional connectivity measures: three non-directional measures—imaginary part of coherency (Nolte et al., 2004), phase-locking value (Lachaux et al., 1999) and amplitude-envelope correlation (Brookes et al., 2011b; O'Neill et al., 2015)—and two directional measures—phase-slope index (Nolte et al., 2008) and frequency-domain Granger causality (Geweke, 1982).

2. Materials and methods

2.1. Head model and sensor layout

The head models used in the simulations were based on the sample anatomy provided with the SimNIBS toolbox (Windhoff et al., 2013). The model data contain FreeSurfer (Dale et al., 1999; Fischl, 2012; Fischl et al., 1999) segmentation of brain, an FSL (Jenkinson et al., 2012) segmentation of skull and skin, and a finite-element volume mesh built based on these segmentations. We used the FreeSurfer-generated mesh for the boundary between white and gray matter (white surface). The rest of the boundaries (pial surface, cerebellum, inner and outer skull, scalp) were extracted from the volume mesh. The original meshes were slightly smoothed according to a desired triangle side length (TSL) (see Table 1) by using the iso2mesh toolbox (Fang and Boas, 2009). Segmentation errors at the head base were manually corrected. The white surface was used for the source space; source-current distributions were modeled using normally-oriented current dipoles placed in the nodes of the mesh. The other meshes were used as conductivity boundaries in a boundary-element volume-conductor model. The same conductivity boundaries had earlier been used for EEG/MEG head modeling by Stenroos and Nummenmaa (2016).

From the mentioned surfaces, we built four head models, which differ by the number of compartments and/or by the mesh sampling. The first model, hereafter referred to as Reference Model (RM), consists of four compartments: brain (i.e., the volume within the pial surface and cerebellum), CSF (i.e., the volume between the pial surface/cerebellum and the inner skull), skull (i.e., the volume between the inner and outer skull surfaces), and scalp (i.e., the volume between the outer skull and the skin surfaces). It was used for generating MEG signals, and as a reference for comparison of forward solutions (see Supplementary Material). Meshes and the head model for RM are visualized in Fig. 1 (see also Stenroos and Nummenmaa, 2016).

The other three models were used for source reconstruction and assessment procedures; for this reason, they will be referred to as Test Models (TMs). The first TM consists of 4 compartments (TM-4c): brain, CSF, skull and scalp. To avoid using exactly the same head model for both

Table 1
Details of the boundary meshes comprising the Reference Model (RM) and the Test Models (TM-4c; TM-3c; TM-1c).

Model name	Mean triangle side length (mm) – Number of triangles					
	White surface	Pial surface	Cerebellum	Inner skull	Outer skull	Skin
RM	3.0–40640	4.0–22592	5.0–1812	5.0–7016	6.0–5388	7.0–5298
TM-4c	3.5–28498	4.0–22592	5.5–1496	5.5–5792	6.5–4578	7.5–4608
TM-3c	3.5–28498	–	–	5.5–5792	6.5–4578	7.5–4608
TM-1c	3.5–28498	–	–	5.5–5792	–	–

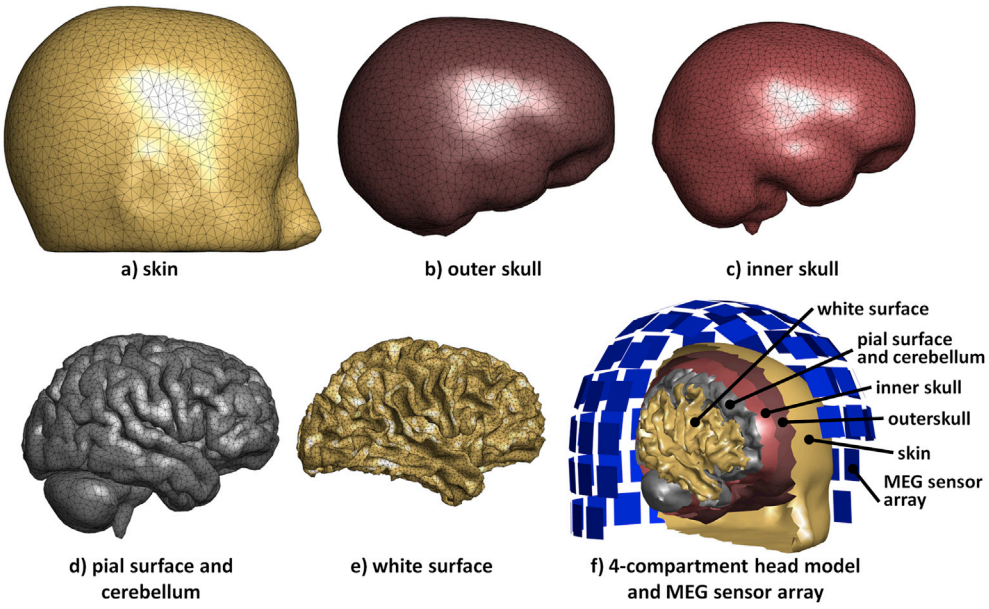

Fig. 1. a–e) Boundary meshes used for the construction of the Reference Model (see also Stenroos and Nummenmaa, 2016), and f) a cross-sectional view of the 4-compartment head model and MEG sensor array.

data generation and assessment procedures, TM-4c was built using a different, slightly coarser cortex mesh (white matter) and smoothed, partially slightly coarser volume meshes obtained by resampling the meshes used for RM. Meshing details for the different head models are listed in Table 1. The second and third TM were obtained as increasingly simplified models from TM-4c. Specifically, the second TM consisted of three compartments (TM-3c): brain, skull, and scalp; it was derived from TM-4c by considering the whole intracranial space, including CSF, as the brain compartment. The third TM consisted of one homogeneous compartment (TM-1c) inside the inner skull surface, coinciding with the innermost compartment of TM-3c. Tissue conductivities in RM and TMs were set equal to $\sigma_{brain} = \sigma_{scalp} = 0.33$ S/m, $\sigma_{skull} = 0.0066$ S/m, and $\sigma_{CSF} = 1.79$ S/m. As MEG is rather insensitive to compartment conductivities, we did not adjust the conductivity of the brain to compensate for the omission of the CSF in TM-3c and TM-1c; such an adjustment would be advisable if EEG were modeled (see Stenroos and Nummenmaa, 2016).

The simulated sensor array comprised 102 magnetometers in the configuration of the 306-channel Elekta Neuromag VectorView system (MEGIN, Helsinki, Finland). The magnetometer output was computed by numerically integrating the field over four points per pick-up coil.

2.2. Simulating co-registration errors

For the generation of the simulated MEG recordings, the head of the RM was almost centered within the MEG helmet, with a minimum head-to-sensors distance of 2.9 cm. In conventional MEG devices, the dewar walls of the MEG helmet are approximately 2 cm thick (as reported in, e.g., Iivanainen et al., 2017); thus the head was reasonably close to the dewar surface, as recommended in real-world measurements.

Imperfect co-registration of TM-4c, TM-3c and TM-1c was then simulated by adding a random translational and rotational error to the head position relative to MEG sensors. The translational error was simulated by a shift to a random direction by distance δ chosen from a normal distribution with zero mean and 5-mm standard deviation. The rotational error consisted of a rotation by an angle θ around a randomly chosen axis (i.e., a randomly oriented axis passing through a randomly chosen point within the head volume), with θ being randomly chosen from a normal distribution with zero mean and 3° standard deviation. Translational and rotational errors were added simultaneously. A total of 250 erroneous co-registrations were generated. After adding the co-registration error, the head position with respect to sensors was verified. In only 11 out of the 250 random repetitions of translations and rotations the minimum head-to-sensors distance was lower than 2 cm; and of these 11 cases, only in one case the minimum head-to-sensors was lower than 1.5 cm (specifically 1.1 cm); in all cases, the sensors were still outside the head.

For each source in the RM, we calculated the source-level co-registration error (SCE) as the distance between the actual source location r_i in the RM and its corresponding misaligned location r_i' in the TMs, i.e.,

$$\mathrm{SCE}_i = \left\| r_i - r_i' \right\| \quad \text{for } i = 1, \ldots, K \,, \tag{1}$$

where $\|\cdot\|$ denotes the Euclidean norm, and i runs over the K sources in RM. Due to different cortical sampling, r_i' does not correspond to any of the possible source locations in the TMs in these models; here, r_i' is calculated by adding the co-registration error to r_i. Based on the above definition, SCE quantifies the error in the knowledge of the actual source location in the misaligned sensor space.

In addition, we defined the cortical co-registration error (CCE) as the

average SCE across all sources, i.e.,

$$\mathrm{CCE} = \frac{1}{K}\sum_{i=1}^{K}\mathrm{SCE}_i\ , \tag{2}$$

2.3. BEM forward modeling

We built forward models for RM and TMs by using a linear collocation boundary-element method (LC-BEM) (de Munck, 1992; Stenroos et al., 2007) formulated with the isolated source approach (Hämäläinen and Sarvas, 1989; Stenroos and Sarvas, 2012). The LC-BEM solver used in this study, called MEGBEM, was verified and used earlier by Stenroos et al. (2014) and by Stenroos and Nummenmaa (2016).

The forward-modeling process results in a lead-field matrix where the i-th column represents the magnetic field generated at the sensors by a unit-strength elementary source, in this case a normally-oriented current dipole, placed at the i-th location of the source space. The lead field matrices for RM and TMs are hereafter distinguished by using plain ($\mathbf{L}$) and 'hatted' ($\widehat{\mathbf{L}}$) symbols, respectively. The co-registration error contributes to the overall difference between the lead fields in the RM and TMs; we refer the interested reader to the Supplementary Material for a detailed analysis of the effects of co-registration errors on the forward models. In the following, we will focus on how this affects the results of source identification and connectivity analysis.

2.4. Generation of synthetic MEG recordings

We simulated a 5-min MEG recording, sampled at 256 Hz, with brain sources and sensor noise. We assumed two interacting sources with unidirectional coupling, i.e., one source is the sender and the other is the receiver. The source time courses, $s_1(t)$ and $s_2(t)$, were generated by using a unidirectional connectivity model in which the first source is a random process, while the second source is influenced, with a delay, by the first source. This model has the form:

$$\begin{cases} s_1(t) = \varepsilon_1(t) \\ s_2(t) = \sum_{p=1}^{P} a(p)s_1(t-p) + \varepsilon_2(t) \end{cases}\ , \tag{3}$$

where $a(p)$ (for $p = 1,\ldots,P$) are linear coefficients describing the time-delayed influence of s_1 on s_2, and ε_i (for $i = 1,2$) are uncorrelated noise terms. Both coefficients and noise terms were sampled from a standard normal distribution. A model order $P = 5$ was used as was done, e.g., in Basti et al. (2018), Haufe et al. (2013), Haufe and Ewald (2016), Nolte et al. (2008) or Sommariva et al. (2017), and the model was tested for stability (Lütkepohl, 2005); we refer to section S3 of the Supplementary Material for further details on the generative model for source time courses. We finally standardized the source time courses for unit variance.

The generated time courses were assigned to two point-like dipolar sources randomly located in the source space. MEG signals were then simulated by multiplying the source time courses with the topography vectors (i.e., the columns of the lead field matrix) for sources at the chosen locations in the RM and adding correlated sensor and biological noise, according to the following model:

$$\mathbf{x}(t) = \mathbf{x}_{\mathrm{i}}(t) + \mathbf{x}_{\mathrm{b}}(t) + \mathbf{x}_{\mathrm{n}}(t), \tag{4}$$

where

$$\mathbf{x}_{\mathrm{i}}(t) = \mathbf{l}_1 s_1(t) + \mathbf{l}_2 s_2(t), \tag{5}$$

is the signal component generated by the interacting sources s_1 and s_2,

$$\mathbf{x}_{\mathrm{b}}(t) = \gamma_1 \sum_{j=1\ldots100} \mathbf{l}_j s_j^{\mathrm{noise}}(t)\ , \tag{6}$$

is the biological noise 'of brain origin' generated by 100 uncorrelated point-like sources uniformly distributed over the cortex, and

$$\mathbf{x}_{\mathrm{n}}(t) = \gamma_2\, \mathbf{n}(t), \tag{7}$$

is normally-distributed sensor noise with fixed covariance matrix taken from a real empty-room MEG measurement (Wakeman and Henson, 2015). In the above notation, $\mathbf{l}_i$ denotes the topography of the i-th source; $s_j^{\mathrm{noise}}(t)$ are the time courses of uncorrelated normally-distributed sources of biological noise; γ_1 and γ_2 are scaling parameters that weight the contribution of biological noise and sensor noise, respectively; and $\mathbf{n}(t)$ is the unweighted vector of sensor noise. We defined the signal-to-biological-noise ratio (SbNR) as the ratio between the root-mean-square (r.m.s.) across sensors of the standard deviation of $\mathbf{x}_{\mathrm{i}}(t)$ and the r.m.s. across sensors of the standard deviation of $\mathbf{x}_{\mathrm{b}}(t)$. Similarly, we defined the signal-to-sensor-noise ratio (SsNR) as the ratio between the r.m.s. across sensors of the standard deviations of $\mathbf{x}_{\mathrm{i}}(t)$ and $\mathbf{x}_{\mathrm{n}}(t)$. For each two-source configuration, we set γ_1 and γ_2 in such a way that $\mathrm{SbNR} = 2$ and $\mathrm{SsNR} = 10$. We also defined the biological-plus-sensor-noise covariance matrix $\mathbf{\Sigma}$ as the covariance matrix of $\mathbf{x}_{\mathrm{b}}(t) + \mathbf{x}_{\mathrm{n}}(t)$.

In order to avoid bias from a particular source configuration or location, we generated 10,000 MEG data sets by independently changing the locations of sources s_1 and s_2 randomly 100 times each (Fig. 2a). In addition, to visualize the obtained results onto the cortical surface, we considered one illustrative case in which s_1 is fixed in the middle frontal cortex (Fig. 2b) while s_2 varies across all the other locations in the source space.

2.5. Source reconstruction

Source time courses were reconstructed from the simulated MEG data sets and forward model from TMs. We recall that, besides being affected by the co-registration error, TMs are different from RM in terms of boundary meshes, spatial sampling and putative source locations, which helped avoid the 'inverse crime' of using the same model parameters for both data generation and source reconstruction (Kaipio and Somersalo, 2007); in addition, the three- and one-compartment TMs also simulate common real-world model simplifications such as the omission of the CSF and the assumption of a homogeneous brain compartment inside the inner skull surface (TM-3c), and the exclusion of the skull and scalp compartments (TM-1c).

Both the simulated data and lead fields from TMs were first pre-whitened with the matrix $\mathbf{\Sigma}^{-1/2}$. That is, we assume that the noise covariance matrix is available, e.g., from a baseline period or a contrast condition. In the following, all signals, topography vectors and lead field matrices are whitened, even though we use the same symbols that we so far used for non-whitened signals and models. We then located the two interacting sources by using a recently developed version of MUltiple SIgnal Classification (MUSIC) algorithm, called Truncated Recursively-Applied-and-Projected MUSIC (TRAP-MUSIC) (Mäkelä et al., 2018). MUSIC-type algorithms aim to estimate source parameters by using the temporal information from the measured signals and the spatial and physical information of the forward model (Mosher and Leahy, 1999, 1998; Schmidt, 1986). In particular, the source localization is performed by evaluating a localizer function at all putative source locations in a scanning grid; the locations of the maxima of the localizer function yield an estimate of source locations. Similarly to conventional RAP-MUSIC algorithms, TRAP-MUSIC allows one to locate multiple sources in a recursive way. Specifically, a plain MUSIC scan is performed at first, yielding an estimate of the first source location (i.e., the global maximum); at each following recursion step, the topography of the source found in the previous step is projected out of the data and the forward model and the dimension of the data and model are reduced by one (Mäkelä et al., 2018); the recursive process is then applied to the

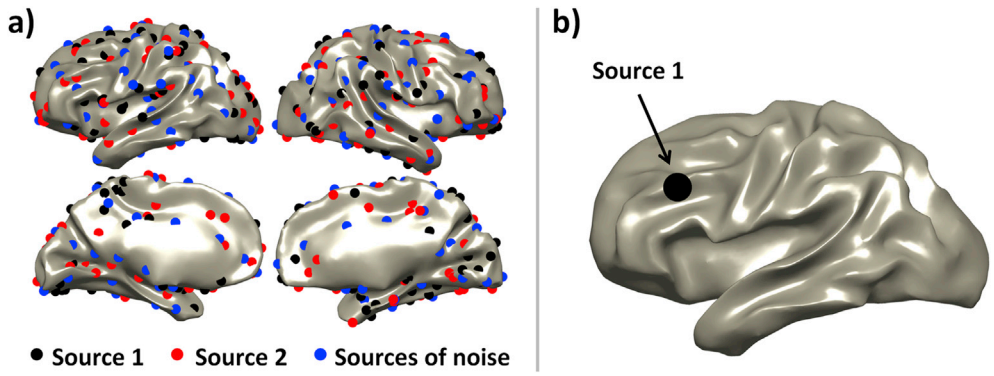

Fig. 2. Locations of the sources used in the generation of simulated MEG data shown on the inflated surface between the white and gray matter. a) The employed 100 source locations for s_1 (black), s_2 (red) and sources of biological noise (blue) randomly chosen from the full source space; b) Sample location of s_1 (black) in the middle frontal cortex for visualizations.

transformed data. Hence the problem of finding multiple local maxima of the localizer in one round is overcome by finding one global maximum at each recursive step. The interested reader is referred to Mäkelä et al. (2018) for details.

The first two maxima of the TRAP-MUSIC localizer yielded an estimate of the location of the two interacting sources. The accuracy of source localization was assessed by using a Source Localization Error (SLE) of the form

$$\mathrm{SLE}_i = \left\| \hat{r}_i - r_i^{'} \right\|, \quad \text{for } i = 1, 2 \tag{8}$$

where $\hat{r}_i$ is the location of source i estimated by TRAP-MUSIC, and $r_i^{'}$ is the actual location in the TM source space as defined in the previous section.

Of note, MUSIC-type algorithms, including TRAP-MUSIC, do not provide the source time courses during the localization process; they need to be estimated separately. For this purpose, we calculated the weight vectors $\widehat{\mathbf{w}}_1$ and $\widehat{\mathbf{w}}_2$ that give an estimate of source time courses at locations $\hat{r}_1$ and $\hat{r}_2$ as a linear combination of sensor signals, i.e.,

$$\hat{s}_i(t) = \widehat{\mathbf{w}}_i\, \mathbf{x}(t), \quad \text{for } i = 1, 2 \tag{9}$$

by using either a scalar linearly constrained minimum-variance (LCMV) beamformer (van Veen et al., 1997) or depth-weighted minimum-norm estimation (MNE) (Hämäläinen et al., 1993; Lin et al., 2004).

In scalar LCMV beamforming, the weight vector $\widehat{\mathbf{w}}_i^{\mathrm{LCMV}}$ of a given source i is estimated by minimizing the variance of $\hat{s}_i(t)$ while satisfying the constraint that the signal that has topography $\widehat{\mathbf{l}}_i$ is passed with unit gain. The solution of this minimization has the form (van Veen et al., 1997)

$$\widehat{\mathbf{w}}_i^{\mathrm{LCMV}} = \left[\widehat{\mathbf{l}}_i^{\mathrm{T}}\, \mathbf{C}_{\mathrm{r}}^{-1}\, \widehat{\mathbf{l}}_i \right]^{-1} \widehat{\mathbf{l}}_i^{\mathrm{T}}\, \mathbf{C}_{\mathrm{r}}^{-1}, \tag{10}$$

where $\widehat{\mathbf{l}}_i$ is the $N \times 1$ topography vector of source i in the TM, $(\cdot)^{\mathrm{T}}$ and $(\cdot)^{-1}$ denote the transpose and inverse operators, respectively, and $\mathbf{C}_{\mathrm{r}}$ is a regularized version of the $N \times N$ measurement covariance matrix $\mathbf{C}$. We use the regularization of the form $\mathbf{C}_{\mathrm{r}} = \mathbf{C} + \mu\boldsymbol{\Sigma}$, where $\boldsymbol{\Sigma}$ is the $N \times N$ noise covariance matrix, and μ is a Backus–Gilbert regularization parameter, in this study set to $\mu = 10$ (Brookes et al., 2011a, 2008). For beamforming, accurate modeling of source space (location and orientation) is important. Overall, if the actual signal topography differs too much from topographies $\widehat{\mathbf{l}}_i$, e.g., due to co-registration errors, due to sources being extended, or head model being too inaccurate, sources are incorrectly reconstructed or even missed.

In MNE, an estimate of distributed source activity that balances between small overall source amplitude, reconstruction of measured signals and rejection of noise is sought (Hämäläinen et al., 1993; Hämäläinen and Ilmoniemi, 1994). The computation of the spatial filter has the form (Lin et al., 2006, 2004)

$$\widehat{\mathbf{W}}^{\mathrm{MNE}} = \mathbf{R}\widehat{\mathbf{L}}^{\mathrm{T}} \left(\widehat{\mathbf{L}}\, \mathbf{R}\, \widehat{\mathbf{L}}^{\mathrm{T}} + \lambda^2 \boldsymbol{\Sigma} \right)^{-1}, \tag{11}$$

where $\boldsymbol{\Sigma}$ is the $N \times N$ noise covariance matrix, $\widehat{\mathbf{L}}$ is the $N \times \widehat{K}$ lead-field matrix of the TMs, and $\mathbf{R}$ is the $\widehat{K} \times \widehat{K}$ source covariance matrix that contains prior information on the source distribution. If no such prior is used, $\mathbf{R}$ is set equal to the identity matrix. The regularization parameter λ^2 that sets the balance between data reconstruction accuracy and source amplitude is commonly set with the help of (power) signal-to-noise ratio SNR^2 (Lin et al., 2006):

$$\lambda^2 = \frac{\mathrm{trace}\left(\widehat{\mathbf{L}}\, \mathbf{R}\, \widehat{\mathbf{L}}^{\mathrm{T}} \right)}{\mathrm{trace}(\boldsymbol{\Sigma})\ \mathrm{SNR}^2}, \tag{12}$$

For each simulated data set, SNR^2 was estimated from the data as the ratio between the trace of the whitened measurement covariance matrix and the trace of the whitened noise covariance matrix; in our case, $\mathrm{trace}(\boldsymbol{\Sigma}) = N$, because our noise covariance matrix had full rank and did not need additional regularization. The weight vector $\widehat{\mathbf{w}}_i^{\mathrm{MNE}}$ of a given source i is finally taken as the i-th row of the matrix $\widehat{\mathbf{W}}^{\mathrm{MNE}}$.

As MNE aims to reconstruct the relevant part of the measurement data with a small overall source amplitude, it favors source locations that produce strong signals. This leads to favoring of superficial tangential sources. For a minimum-norm spatial filter this means strong response (cross-talk) from those superficial sources. This property may be mitigated by so-called depth weighting, namely by multiplying the elements of $\mathbf{R}$ corresponding to the i-th source by

$$f_i = \left(\widehat{\mathbf{l}}_i^{\mathrm{T}}\, \widehat{\mathbf{l}}_i \right)^{-q} \tag{13}$$

where q is a tunable depth-weighting parameter, whose optimal value depends on several factors, including decimation of the source space, local anatomy features, and the regularization parameter. In this study, we used $q = 0.4$ based on a preliminary quantitative analysis that we performed as suggested by Lin et al. (2006). Thus, we set $\mathbf{R}$ to a diagonal matrix, with values f_i on the diagonal.

We assessed the accuracy of source activity estimates by using the Crosstalk-to-Signal Ratio (Cho et al., 2015; Sekihara and Nagarajan, 2008) and the Neural Activity Index (van Veen et al., 1997). The Crosstalk-to-Signal Ratio (CSR) is a measure of the contamination induced in the estimated activity of one source due to the activity of the other source, and it is expressed as

$$\mathrm{CSR}_1 = \frac{\left| \widehat{\mathbf{w}}_1\, \mathbf{l}_2 \right|}{\left| \widehat{\mathbf{w}}_1\, \mathbf{l}_1 \right|}, \tag{14}$$

for source 1, and

$$\mathrm{CSR}_2 = \frac{|\widehat{\mathbf{w}}_2\, \mathbf{l}_1|}{|\widehat{\mathbf{w}}_2\, \mathbf{l}_2|}, \tag{15}$$

for source 2, where $|\cdot|$ denotes the absolute value. A non-zero CSR indicates the presence of zero-lag correlated components in the reconstructed source time courses, which are due to the leakage of one source time-course into the estimate of the other source; this is often referred to as the source-leakage effect (Brookes et al., 2012; Colclough et al., 2016). The Neural Activity Index (NAI) quantifies, for each source, the ratio between the reconstructed source power and projected noise power, and it is given by

$$\mathrm{NAI}_i = \frac{\widehat{\mathbf{w}}_i\, \mathbf{C}\, \widehat{\mathbf{w}}_i^{\mathrm{T}}}{\widehat{\mathbf{w}}_i\, \mathbf{\Sigma}\, \widehat{\mathbf{w}}_i^{\mathrm{T}}}, \qquad \text{for } i = 1, 2. \tag{16}$$

Small NAI values mean that the reconstructed source time-courses contain a large amount of noise, which is likely to render connectivity between the reconstructed sources invisible.

2.6. Connectivity analysis

Connectivity was estimated from the time courses of the reconstructed sources, $\widehat{s}_1(t)$ and $\widehat{s}_2(t)$, by using five different connectivity measures. Three of them were non-directional measures: imaginary part of coherency (ImCohy) (Nolte et al., 2004), phase-locking value (PLV) (Lachaux et al., 1999) and amplitude-envelope correlation (AEC) (Brookes et al., 2011b; O'Neill et al., 2015); and the two others directional measures: phase-slope index (PSI) (Nolte et al., 2008) and frequency-domain Granger causality (fGC) (Geweke, 1982). Basic principles and estimation methods for these measures are available in Section S2 of Supplementary Material.

Source-leakage effects represent a potential confound in the MEG source connectivity analysis. They result in zero-phase-lag correlation between the reconstructed source time courses that, without careful control, can artifactually inflate the estimated connectivity (Basti et al., 2018, 2017; Brookes et al., 2012; Chella et al., 2016, 2014; Colclough et al., 2016; Ewald et al., 2012; Hipp et al., 2012; Marzetti et al., 2013; Nolte et al., 2004; Palva et al., 2018; Soto et al., 2016; Vinck et al., 2011). Among the connectivity measures investigated in this study, ImCohy and PSI are robust to this bias since zero-phase-lag effects are inherently removed (Nolte et al., 2008, 2004); similarly, fGC is not inflated by the leakage of one source to the other. However, PLV and AEC are affected by source leakage, and therefore, prior to the estimation of connectivity, we applied a source-leakage compensation by using a pairwise orthogonalisation procedure (Brookes et al., 2012; O'Neill et al., 2015) for band-limited signals.

In order to investigate the effects of co-registration errors on the above connectivity measures, we restricted our analysis to the frequency range 8–12 Hz to mimic a realistic scenario of data analysis. AEC was computed after frequency filtering the source time courses to this range. The other measures were computed in the frequency domain for frequencies in this range with 1-Hz steps, and then averaged over the band. ImCohy and AEC, which may be negative-valued, were considered as absolute values, in such a way that a decrease of their value unambiguously indicates a decrease of estimated connectivity.

We assessed the accuracy of the obtained estimates for each connectivity metric (ImCohy, PLV, AEC, PSI, or fGC) by using a Relative Error (RE) measure defined as

$$\mathrm{RE} = \frac{|\mu_{12} - \mu_{12}^{\mathrm{true}}|}{|\mu_{12}| + |\mu_{12}^{\mathrm{true}}|}, \tag{17}$$

where μ_{12} is the estimated value, i.e., obtained from the reconstructed source time courses, and μ_{12}^{true} is the true value, i.e., obtained directly from source time courses used in the generation of simulated data. The RE is a normalized difference between the estimated and the true value, with the normalization ensuring RE to be bound between 0 and 1. In addition, to map relative errors onto the cortical surface, we calculated a *signed* Relative Error (RE) by omitting the absolute value at the numerator of the above formula, i.e., we kept the sign of the difference between the estimated value and the true value, in such a way that a positive *signed* RE value indicates a locally inflated connectivity estimate, while a negative *signed* RE value indicates a locally deflated connectivity estimate.

Statistical analysis for the contrast between RE distributions obtained by using the three different head models in forward solution (TM-4c, TM-3c, or TM1-c) was carried out by using a non-parametric Friedman test, followed by a Tukey post-hoc test. Correction for multiple comparison was performed using the false-discovery-rate (FDR) approach (Benjamini and Yekutieli, 2001). For pairwise comparisons between RE distributions obtained by using two different head models, or by using the two different source reconstruction techniques (beamforming or MNE), we relied on a non-parametric Wilcoxon signed-rank test. We also calculated the effect size **r** associated to Wilcoxon *z*-value as $\mathbf{r} = \mathrm{z}/\sqrt{n}$, where n is the number of samples (Fritz et al., 2012). By convention, **r**-values of 0.1, 0.3, and 0.5 are considered 'small', 'medium', and 'large' effect sizes, respectively (Cohen, 1988).

2.7. Data and code availability statement

The code used for synthetic data generation and analysis is available upon direct request.

3. Results

3.1. Assessment of source reconstruction

SLE for TRAP-MUSIC source localization, as well as CSR and NAI for both beamforming and MNE source activity reconstruction, were first evaluated for sources s_1 and s_2 separately, and for all simulation repetitions obtained by randomizing source locations. CSR and NAI, which quantify relative amplitude and power measures, respectively, were logarithmically transformed. We then averaged these indices across sources s_1 and s_2, and sorted the obtained values for increasing mean source co-registration error across s_1 and s_2 in the range 0–15 mm, i.e., a range which matches expected and reported real co-registration errors (Hillebrand and Barnes, 2011; Whalen et al., 2008); with this range selection, we retained roughly the 98% of total cases generated in simulation. CSR values were also sorted as a function of the distance between s_1 and s_2.

Fig. 3 shows the box plots of the distribution of SLE as a function of the mean source co-registration error between sources s_1 and s_2. We first note that SLE increases for an increasing co-registration error. In particular, for a mean source co-registration errors ranging from 0 to 15 mm, the median SLE values range from 1 to 3 mm, depending on the forward model accuracy, up to about 15 mm. Overall, head model simplifications, i.e., the omission of CSF in TM-3c and the further exclusion of skull and scalp in TM-1c, cause an increase of the SLE, but the differences between the TMs rapidly decrease for increasing co-registration error.

Fig. 4 shows the median logarithmic CSR as a function of the mean source co-registration error (x axis) and of the distance between sources s_1 and s_2 (y axis). Of note, CSR is relevant only for nearby sources, and it rapidly decreases for increasing distance between sources. For instance, a $\log_{10}$(CSR) equal to -1 means that the source contamination from cross-talk is one tenth of the true source signal, which at low co-registration errors (<3 mm) occurs for s_1-to-s_2 distance lower than ~10 mm (for TM-4c) or ~20 mm (for TM-3c and TM-1c) in beamforming, or lower than ~50 mm in MNE. Interestingly, CSR shows a clear dependence on co-registration errors only for sources reconstructed using beamforming, with the cross-talk decaying less rapidly with source distance for

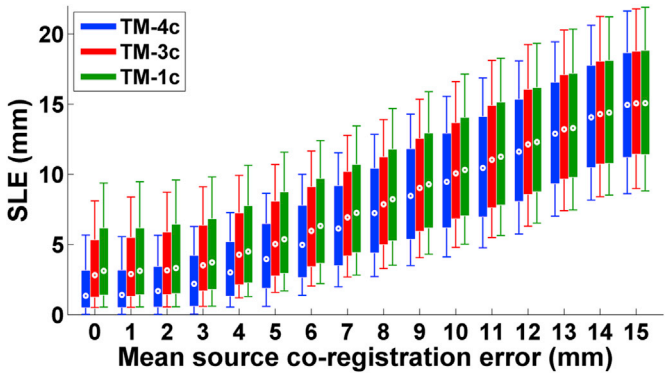

Fig. 3. Box plots for Source Localization Error (SLE) as a function of the mean source co-registration error across s_1 and s_2, for source locations estimated by using TRAP-MUSIC. The dot, the rectangular box and the whiskers for each box plot denote the median value, the range from the 16th to the 84th percentile and the range from the 5th to the 95th percentile of the distribution, respectively. Notice that these roughly correspond to the mean value and the ranges between one or two standard deviations below and above the mean in case of Gaussian distribution. The abscissa is divided into bins (i.e., intervals) of 1-mm width, and each box plot is displayed on the right-hand edge of the corresponding bin – i.e., the box plot at 1 mm collects the data for mean source co-registration error between 0 (excluded) and 1 mm (included), the box plot at 2 mm collects the data for mean source co-registration error between 1 (excluded) and 2 mm (included), and so on; the box plot at 0 mm corresponds to the case of no co-registration error. In blue: data obtained using the 4-compartment test model (TM-4c). In red: data obtained using the 3-compartment test model (TM-3c). In green: data obtained using the 1-compartment test model (TM-1c).

increasing co-registration errors. No noticeable effects can be observed when using MNE, although it must be noted that the CSR decays less rapidly with source distance than in beamforming, at least if the co-registration error is low. Analogously to SLE, small changes in CSR due to the head model simplification can be observed only for beamforming-reconstructed sources and if the co-registration error is small.

Fig. 5 shows the box plots of the distribution of logarithmic NAI as a function of the mean source co-registration error. Analogously to CSR, NAI shows a dependence on co-registration error only for sources reconstructed using beamforming, with NAI rapidly decreasing for increasing co-registration error. Specifically, for mean source co-registration errors ranging from 0 up to 15 mm, the median NAI values range from ~1.5 (i.e., for TM-4c) or ~1.3 (i.e., for TM-3c and TM-1c) to ~0.9 (i.e., for all TMs). No noticeable dependence of NAI values on co-registration error can be observed for sources reconstructed using MNE. Finally, for beamforming-reconstructed sources, NAI values obtained using TM-3c and TM-1c are systematically lower than the ones obtained using TM-4c, although the difference decreases for increasing co-registration error.

3.2. Assessment of source connectivity estimates

RE values were computed for all simulation repetitions, and then sorted for ascending mean co-registration error across sources s_1 and s_2. The obtained RE distributions are plotted in Fig. 6. In this figure, the panels in different rows refer to different connectivity measures (PLV, ImCohy, AEC, PSI, and fGC), while the panels in different columns refer to different source reconstruction technique (left column for beamforming; right column for MNE).

For beamforming (Fig. 6, left column), we first note that the RE values increase for increasing co-registration error, with median values ranging from a few percent in case of zero-error up to about 7–8% for PLV and ImCohy, or even about 15–20% for AEC, PSI and fGC, in case of 15-mm error. A more marked increase can be observed at the upper tails of the distributions, denoted by the 84th and 95th percentiles, especially for directional measures (PSI and fGC). In order to quantify the impact of an improved co-registration on the accuracy of connectivity estimates obtained with beamforming, we compared the mean values of RE for three different ranges of mean source co-registration error (mSCE): 0 mm $\leq$ mSCE $\leq$ 3 mm (low mSCE), 3 mm $<$ mSCE $\leq$ 7 mm (medium mSCE), and 7 mm $<$ mSCE $\leq$ 15 mm (high mSCE). The obtained results are listed in Table 2a–c. Here, we also list the ratio of mean RE values in high mSCE and medium mSCE to low mSCE, which quantifies the factor that we expect to gain in the accuracy of connectivity estimates by reducing the co-registration error below 3 mm. Notably, on average this factor is about 1.5 (for TM-4c) or 1.3 (for TM-3c and TM-1c) when switching from medium to low mSCE, and about 2.6 (for TM-4c) or 1.9 (for TM-3c and TM-1c) when switching from high to low mSCE.

For beamforming-based connectivity estimates (Fig. 6, left panels), we also observe that RE values obtained for TM-3c and TM-1c are systematically larger than the respective values obtained for TM-4c for small co-registration errors, which demonstrates a systematic decrease in the accuracy of connectivity estimates when a simplified volume-conductor model is used. Moreover, RE values for TM-3c and TM-1c show little difference as compared to those of TM-4c. A non-parametric Friedman test performed to compare different TMs, followed by a Tukey post-hoc

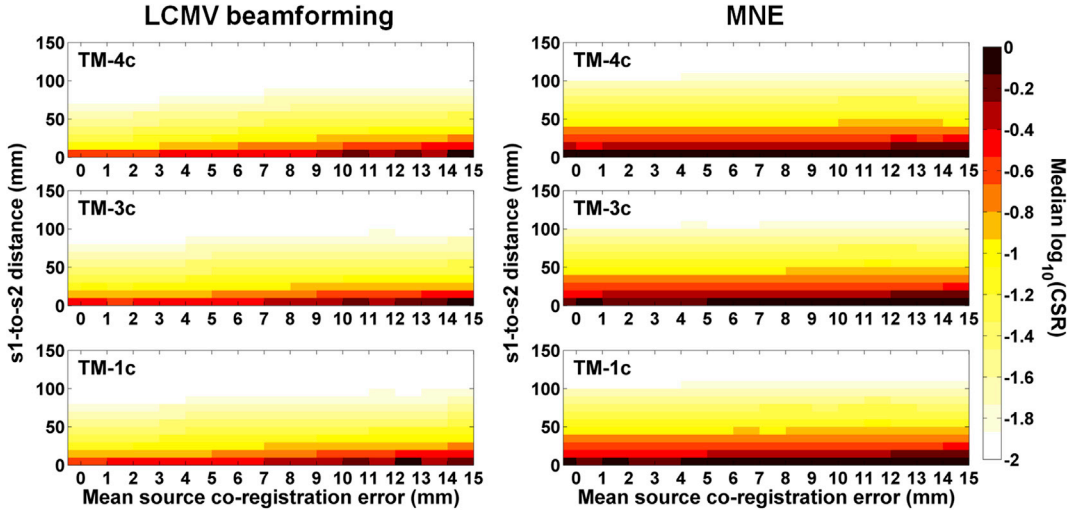

Fig. 4. Heat maps for the median logarithmic Crosstalk-to-Signal Ratio, $\log_{10}$(CSR), as a function of the mean source co-registration error across s_1 and s_2 and of the distance between s_1 and s_2, obtained using three different test models (top row: TM-4c; middle row: TM3-c; bottom row: TM-1c) and two different source reconstruction methods (left column: LCMV beamforming; right column: MNE).

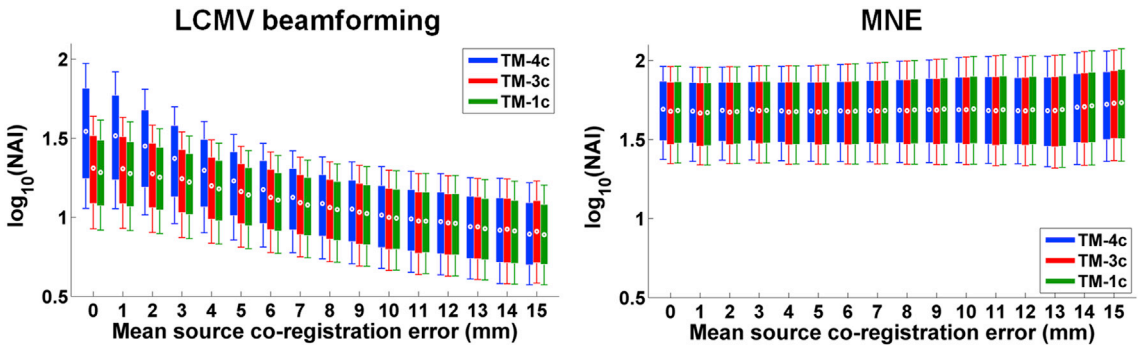

Fig. 5. Box plots for logarithmic Neural Activity Index, $\log_{10}$(NAI), as a function of the mean source co-registration error across s_1 and s_2, for sources reconstructed by using a beamforming approach (LCMV beamforming, left panel) and a weighted MNE solution (MNE, right panel). NAI quantifies the ratio between reconstructed source power and projected noise power, in such a way that large NAI values mean that the reconstructed source time courses contain a small amount of noise. The dot, the rectangular box and the whiskers for each box plot denote the median value, the range from the 16th to the 84th percentile and the range from the 5th to the 95th percentile of the distribution, respectively. Notice that these roughly correspond to the mean value and the ranges between one or two standard deviations below and above the mean in case of Gaussian distribution. The abscissa is divided into bins (i.e., intervals) of 1-mm width, and each box plot is displayed on the right-hand edge of the corresponding bin—i.e., the box plot at 1 mm collects the data for mean source co-registration error between 0 (excluded) and 1 mm (included), the box plot at 2 mm collects the data for mean source co-registration error between 1 (excluded) and 2 mm (included), and so on; the box plot at 0 mm corresponds to the case of no co-registration error. *In blue*: data obtained using the 4-compartment test model (TM-4c). *In red*: data obtained using the 3-compartment test model (TM-3c). *In green*: data obtained using the 1-compartment test model (TM-1c).

test, with FDR correction, revealed a significant effect of head-model accuracy on RE values, even if some of the differences that can be observed in Fig. 6 are small (see section S4 of the Supplementary Material for summary tables of test statistics). We considered this as an effect due to the large sample size, given by the number of simulated source pairs (minimum sample size: 10,000 at mSCE = 0 mm; degrees of freedom for groups and error: 2; 19,998). This also means that the large variability observed in the RE distributions is mainly due to the within-group variability, i.e., across the different source pairs (our units-of-observation). We then performed pairwise contrasts between different TMs by using a non-parametric Wilcoxon signed-rank test, and we evaluated meaningful differences by using the associated effect size **r**. Fig. 7a–c shows the effect size as a function of the mean source co-registration error for the difference TM-3c–TM-4c, TM-1c–TM-4c and TM-3c–TM-1c, respectively. In this figure, conventional values for a small (0.1), medium (0.3), and large (0.5) effect size have been marked by the horizontal grid lines. Notably, for PLV, ImCohy, AEC and fGC, the effect size between TM-4c and TM-3c (Fig. 7a) or TM-1c (Fig. 7b) is large below a mean co-registration error between 3 and 5 mm, or medium-to-large below a mean co-registration error between 5 and 7 mm, depending on the connectivity measure. Above this limit, the effect size rapidly decays toward small values; for PSI, the effect size is substantially smaller, being medium-to-large only below 4 mm. The effect size between TM-3c and TM-1c (Fig. 7c) is overall small or negligible in a wide range of co-registration errors, i.e., 0–15 mm.

Regarding connectivity estimated from sources reconstructed using MNE (Fig. 6, right panels), we note that there are no noticeable effects of co-registration errors on RE for connectivity estimates. For a direct comparison with the RE values obtained using beamforming, we compared the RE distributions obtained by the two source reconstruction techniques by using a Wilcoxon signed-rank test with FDR correction. Specifically, we will refer here only to the case when a 4-compartment head model (TM-4c) is used. Similarly to the Friedman test, due to the large sample size, we assessed meaningful differences between RE distributions by using Cohen's effect size **r**. Fig. 7d shows the effect size for the difference $RE_{MNE} - RE_{beamforming}$ as a function of the mean source co-registration error. We found that for directional measures (fGC and PSI) the RE for MNE is larger than the RE for beamforming below a co-registration error of about 6 mm, but the effect size is small-to-medium only below 2 or 3 mm; above 3 mm, the RE for MNE is smaller than the RE for beamforming, with the effect size rapidly increasing (in absolute value) for increasing co-registration error. For non-directional measure (PLV, ImCohy and AEC), we found small difference between the RE distributions below a co-registration error of about 2 mm; whilst above this limit, the RE for beamforming becomes substantially larger (negative effect size) than the RE for MNE.

We finally investigated the spatial features of the effects of co-registration errors on connectivity estimates by mapping the relative errors onto the cortical surface. As MNE did not show clear effects due to co-registration error, we will only discuss the case in which LCMV beamforming is used for source reconstruction. For the visualization of cortical maps, we considered an illustrative case in which source s_1 is fixed at a given location in the middle frontal cortex (see Fig. 2), while the location of the source s_2 varies across all the possible locations in the source space. We then evaluated relative errors for connectivity measures and plotted these values at the location of source s_2.

The cortical maps of signed RE were averaged on the basis of the cortical co-registration error (CCE) (i.e., the mean source co-registration error over the cortex; see Eq. (2)) into three ranges: 0 mm $\leq$ CCE $\leq$ 3 mm (low CCE), 3 mm $<$ CCE $\leq$ 7 mm (medium CCE), and 7 mm $<$ CCE $\leq$ 15 mm (high CCE). Fig. 8 shows the maps of the average *signed* RE in the low, medium and high CCE range, obtained from TM-4c. We observe two main effects. First, there is an overall negative *signed* RE all over the brain, being largest at gyrus top and deep regions, especially insula, which demonstrates a decrease of the estimated connectivity with respect to the true value; such a decrease is enhanced by a larger co-registration error. Second, there is substantial decrease in an area surrounding the location of s_1; also this effect is enhanced by a larger co-registration error, but is more marked for directional measures (PSI and fGC). A similar pattern for the *signed* RE was observed for TM-3c and TM-1c (data not shown here).

4. Discussion

In this study, we investigated the impact of improved MEG–MRI co-registration strategies, which promise unprecedented accuracy, on MEG source-level connectivity estimates. The results were achieved using extensive simulations in which synthetic MEG data sets were generated for pairs of connected brain sources at variable locations. From these, the capability of estimating source connectivity, as measured by ImCohy, PLV, AEC, PSI and fGC, was assessed for co-registration errors of 0–15 mm and for four-, three- and one-compartment volume-conductor models. This was tested for two widely used source-reconstruction techniques: LCMV beamforming and MNE. Overall, our findings

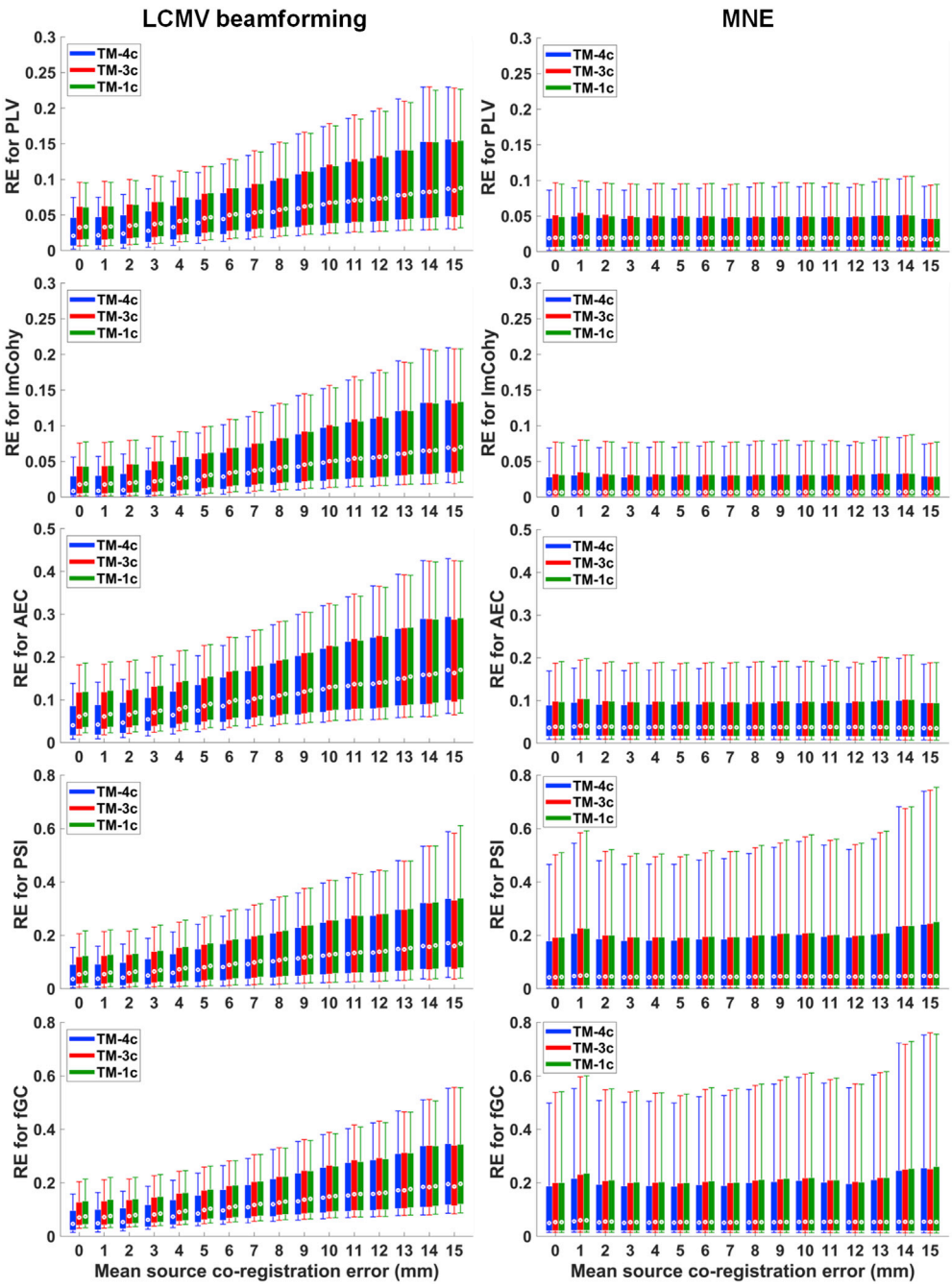

Fig. 6. Box plots for Relative Error (RE) for connectivity estimates as function of the mean source co-registration error across s_1 and s_2. The panels in different rows refer to different connectivity measures (PLV, ImCohy, AEC, PSI, and fGC), while the panels in different columns refer to different source-reconstruction techniques (left-column for beamforming; right-column for MNE). *In blue*: data obtained using the 4-compartment test model (TM-4c). *In red*: data obtained using the 3-compartment test model (TM-3c). *In green*: data obtained using the 1-compartment test model (TM-1c).

suggest that the beamforming approach (LCMV) can better take advantage of accurate co-registration than MNE. This was the case of all the investigated connectivity methods. On the other hand, MNE provides more stable results in a wide range of co-registration errors, i.e., from 0 to 15 mm, while the performance of beamforming rapidly degrades for increasing co-registration errors. In particular, for beamforming-reconstructed sources, our results suggest that the accuracy of connectivity estimates in routine MEG analysis can be increased by a factor between 1.3 and 2.2 if the co-registration error is kept below 3 mm, or even by a factor between 1.5 and 3.1 if a detailed head model is available (see Table 2).

It is important to understand the two effects of co-registration errors on connectivity estimates obtained from sources reconstructed by using beamforming. First, there is an overall decrease in the values of connectivity metrics for increasing co-registration errors (Figs. 6 and 8) due to source attenuation and relative increase of noise contamination in reconstructed source activity (Fig. 5, left panel). Such a decrease was observed for all the investigated connectivity metrics, being largest for directional metrics (i.e., PSI and fGC). This is conceivably due to a strict spatial constraint of the beamforming, namely if the topographies of putative sources get far apart from the topographies of the actual sources, the amount of projected source signal decreases, or even vanishes at large distances, while the projected noise amplitude does not change significantly. This was confirmed by the fact that, as shown in Fig. 8, the decrease is largest at the top of the gyrus. At these locations, sources are close to radial with respect to skull and thus produce weak magnetic fields; in these conditions, already a small change in source orientation may cause a large relative change in the field (see also Supplementary Material). In this respect, beamforming is known to be highly sensitive to inaccurate lead-field modeling (van Veen et al., 1997), especially if the

Table 2
Mean Relative Error (RE) for connectivity estimates (PLV, ImCohy, AEC, PSI, or fGC) obtained with beamforming for three ranges of mean source co-registration error (mSCE): 0 mm ≤ mSCE ≤ 3 mm (low mSCE), 3 mm < mSCE ≤ 7 mm (medium mSCE), and 7 mm < mSCE ≤ 15 mm (high mSCE). (a) Data obtained when using a 4-compartment test model (TM-4c). (b) Data obtained when using a 3-compartment test model (TM-3c). (c) Data obtained when using a 3-compartment test model (TM-1c). For each test model, the ratio of mean RE values in high mSCE and medium mSCE to low mSCE is also given.

a) TM-4c	Low mSCE	Medium mSCE	High mSCE	Medium mSCE / Low mSCE	High mSCE / Low mSCE
PLV	0.03	0.05	0.08	1.50	2.39
ImCohy	0.02	0.03	0.06	1.71	3.08
AEC	0.06	0.09	0.15	1.49	2.34
PSI	0.06	0.10	0.16	1.53	2.53
fGC	0.07	0.11	0.18	1.50	2.41
b) TM-3c	Low mSCE	Medium mSCE	High mSCE	Medium mSCE / Low mSCE	High mSCE / Low mSCE
PLV	0.04	0.06	0.08	1.28	1.84
ImCohy	0.03	0.04	0.06	1.39	2.20
AEC	0.08	0.11	0.15	1.27	1.83
PSI	0.08	0.11	0.16	1.32	1.99
fGC	0.10	0.13	0.18	1.28	1.87
c) TM-1c	Low mSCE	Medium mSCE	High mSCE	Medium mSCE / Low mSCE	High mSCE / Low mSCE
PLV	0.04	0.06	0.08	1.28	1.83
ImCohy	0.03	0.04	0.06	1.39	2.17
AEC	0.09	0.11	0.15	1.25	1.76
PSI	0.09	0.11	0.17	1.30	1.91
fGC	0.10	0.13	0.18	1.27	1.82

SNR is high, i.e., when the noise does not cover the differences between the actual and modeled lead fields (Boto et al., 2016; Hillebrand and Barnes, 2003). The above results are consistent with the recent findings from Liuzzi et al. (2017) that showed that co-registration errors have the effect of reducing the magnitude of functional connectivity estimated from beamforming-reconstructed sources, as well as the effect of increasing the variability of connectivity estimates over simulated recordings.

Second, there is a substantial decrease in the estimated connectivity between nearby sources (Fig. 8). This effect is most likely a result of the limited spatial resolution related to the so-called leakage or cross-talk problem in reconstructed source activity (see also Hauk and Stenroos, 2014). This is confirmed by the results in Fig. 4 (left panel), which indeed show increasing cross-talk between nearby sources for increasing co-registration errors. In this study, we compensated for spatial leakage using either connectivity measures which are not biased by zero-phase-lag correlations or a signal orthogonalization procedure prior to the estimation of connectivity. Such measures can reduce but not completely suppress the bias arising from source leakage. This bias was found to be especially relevant for directional measures (PSI and fGC) and it increased with the co-registration error.

The above effects were present even though beamformers reconstructed the source time courses at locations which maximized the TRAP-MUSIC localizer. One reason for this is that the effects of co-registration error are global; co-registration errors affect not only the grid locations relative to MEG sensors but also the orientations of cortical surface normals as well as the location and orientation of the whole volume-conductor model used for source estimation. In our data, this is reflected by the difference between the true lead fields and the modeled lead fields (see the Supplementary Material); such a difference increases for increasing co-registration error (Fig. S1 of the Supplementary Material) and it affects almost all the grid locations (Fig. S3 of the Supplementary Material) including those selected for source time course estimation. As discussed above, this causes errors in beamformer source reconstruction and related connectivity estimates, which, analogously to lead-field modeling errors and localization accuracy (Fig. 3), increase for increasing co-registration error.

Our results show that, contrarily to beamforming, MNE provides time-course and connectivity estimates that are not very sensitive to co-registration errors, at least in the error range investigated in the present study. This is because MNE spatial filter has distributed and rather smooth spatial sensitivity profile, which is a consequence of the *l*2-norm minimization employed in derivation of the solution. The spatial smoothness of MNE makes it thus more tolerant to small displacements of head position relative to sensors. In our simulations, the smoothness leads to overall larger cross-talk between sources compared to typical beamforming solutions (Fig. 4, right panel). The interpretation of this observation is non-trivial. Promoting smoothness to alleviate the effects of co-registration errors might favor sources which are far from one another, whereas on the contrary, care should be taken if two sources are close to one another, since residual signal-leakage effects would unavoidably affect the connectivity estimates. Our simulation setting, however, favors beamforming, because we use two point-like dipoles for simulations and the LCMV beamformer scans the source space with

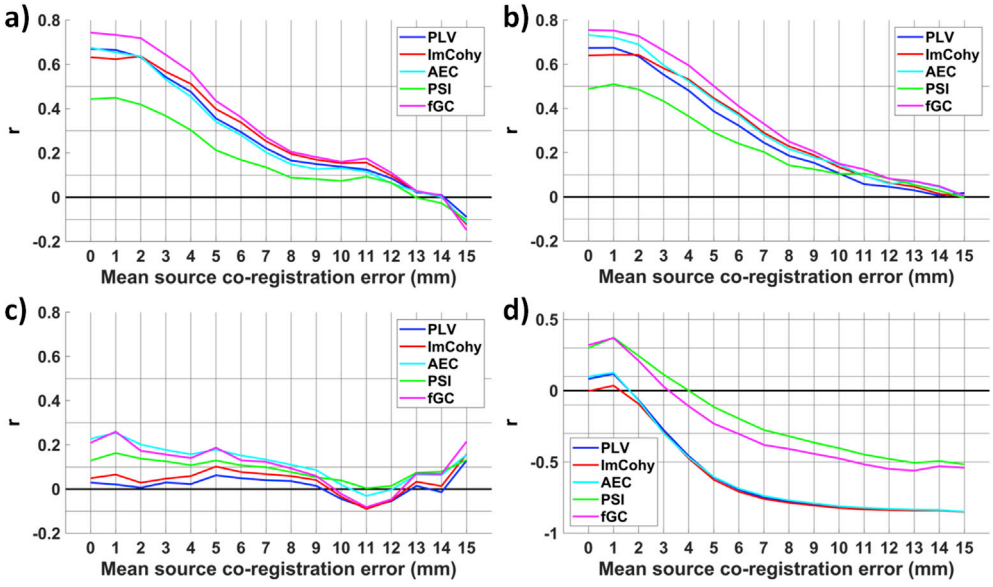

Fig. 7. a–c) Effect size **r** for the difference between RE distributions obtained by using different TMs (i.e., a) $RE_{TM\text{-}3c} - RE_{TM\text{-}4c}$; b) $RE_{TM\text{-}1c} - RE_{TM\text{-}4c}$; c) $RE_{TM\text{-}1c} - RE_{TM\text{-}3c}$) with beamforming source reconstruction, as a function of the mean source co-registration error. d) Effect size **r** for the difference between RE distributions obtained by using different source reconstruction techniques, i.e., $RE_{MNE} - RE_{beamforming}$, with TM-4c, as a function of the mean source co-registration error. Conventional values for a small (0.1), medium (0.3), large (0.5) effect size have been marked by the horizontal grid lines. Different colored lines refer to different connectivity measures (PLV, ImCohy, AEC, PSI, fGC).

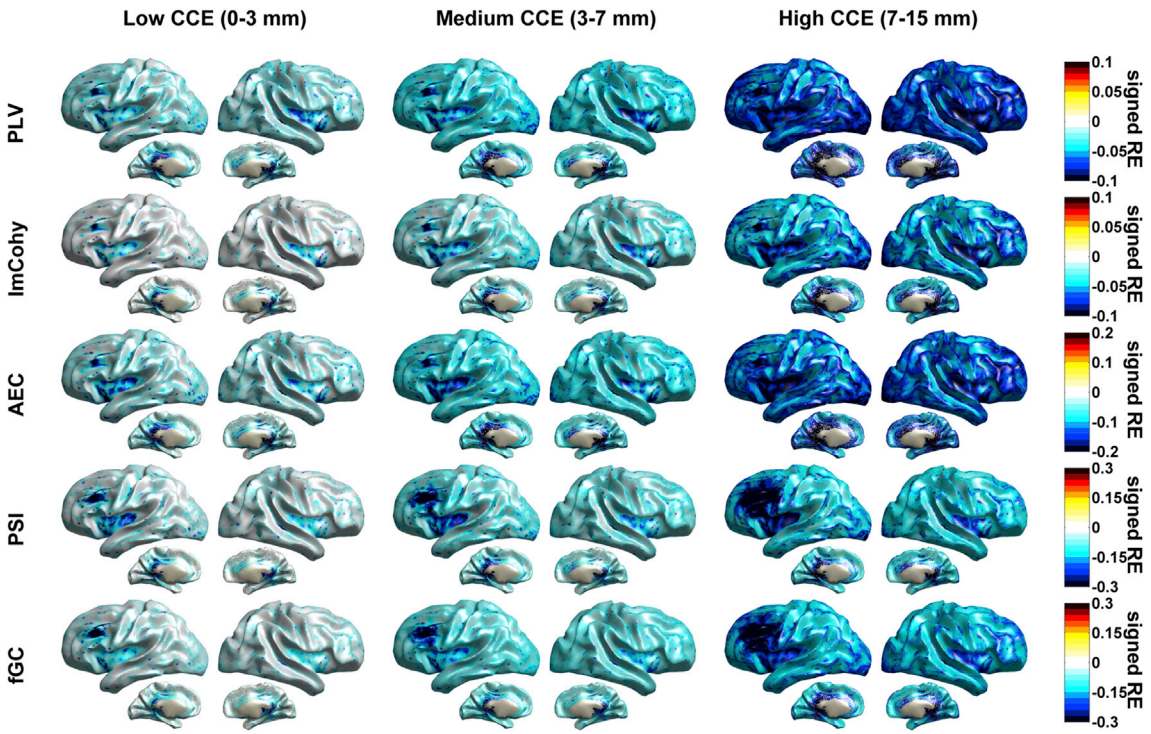

Fig. 8. Maps of the average *signed* Relative Error (RE) for different connectivity measures (first, second and third row: non-directional measures, i.e., PLV, ImCohy and AEC; fourth and fifth row: directional measures, i.e., PSI and fGC) for an illustrative case in which s_1 is located in the middle frontal gyrus. The maps are plotted on the inflated boundary surface between the white and gray matter, and they show the average *signed* RE in three different CCE ranges (*left column*: low CCE = 0–3 mm; *middle column*: medium CCE = 3–7 mm; *right column*: high CCE = 7–15 mm). Data obtained from TM-4c.

point-like dipoles and thus performs ideally with a data comprising a small set of dipolar sources (van Veen et al., 1997), while the MNE spatial filter attempts to reject cross-talk globally, not getting any advantage from the sparse nature of our simulated data (see Hauk and Stenroos, 2014). Our use of different volume conductor models and slightly different source positions and orientations for reference and test models alleviates this bias.

Our results suggest that, in our simulated conditions, if the co-registration error is below 3 mm, a beamforming approach provides more accurate estimates of directional connectivity measures (PSI and fGC), while a small difference was observed for non-directional connectivity measures (PLV, ImCohy, AEC) (Fig. 7d). Above this limit, the performance of beamforming over inaccurately modeled sources becomes worse than that of the minimum-norm estimate.

We simulated our data using a four-compartment model and estimated connectivity using a four-compartment, as well as a three- and one-shell models, and observed that simplifications of the volume-conductor model (i.e., the omission of CSF in TM-3c, with the exclusion of skull and scalp in TM-1c) decreased the accuracy of connectivity estimates when beamforming was used. Such a decrease was, however, relevant only if the co-registration error was lower than a value between 4 and 7 mm, depending on the connectivity measure (Fig. 7a–b). Hence, the importance of precise co-registration increases if one wants to take full advantage of highly accurate head models. Highly detailed head models are rarely employed in MEG for practical reasons such as the time and effort required for such model construction (e.g., extra MRI sequences, segmentation, uncertainties in modeling conductivity and anisotropy, etc.). Recent software developments and technical solutions are, however, overcoming part of these issues so that highly accurate head models might gain in the future a more widespread use in MEG practice (Lew et al., 2009; Stenroos and Nummenmaa, 2016). Based on our findings, we then posit that novel co-registration strategies will be beneficial for the effective use of these models.

In order to achieve a practical relevance of our results, we tested realistic head models and MEG sensor configuration. In particular, a realistically-shaped four-compartment head model was used as a reference model, which is anatomically more accurate than the conventionally used three- and one-compartment models and allows easy testing of the effects of common model simplifications. The simulated data were generated with dense boundary meshes for BEM and a cortical model with about 20,000 source locations, while source reconstruction was performed by using smoothed boundary meshes for BEM and a cortical model with about 14,000 source locations. Hence, our results are not likely to be affected by the inverse crime of using the same head model for the forward and inverse steps (Kaipio and Somersalo, 2007). Nevertheless, like in most simulation studies, our simulations are biased in favor of the higher-detail test model: most importantly, both the reference model and the high-detail test model had the same four compartments and conductivities. Further, the reference and test models were built from the same original segmentations, and thus all the added anatomical information in the four-compartment test model was correct (apart from smoothing and remeshing). One should thus not read our results as "the effect of simplifying the head model", but rather as an overall comparison between near-ideal and real-world forward models (see also Stenroos and Nummenmaa, 2016).

For the sake of completeness, it should be noted that, in this study, we restricted ourselves to the evaluation of the effects of co-registration errors on a limited number of connectivity measures. In particular, we chose five well-established measures of connectivity: three non-directional measures (ImCohy, PLV and AEC) and two measures which are specifically designed to detect directional couplings (PSI and fCG). Yet, there is a wide family of connectivity measures which could be used to assess functional and effective coupling in oscillatory brain activity, occurring both at the same or at different frequencies (e.g., Bastos and Schoffelen, 2016; Chella et al., 2014; Darvas et al., 2009; O'Neill et al., 2015; Özkurt, 2016; Pereda et al., 2005; Tass et al., 1998). While testing all possible variants of such connectivity metrics is beyond the scope of this work, we might still reasonably argue that co-registration errors will

have a similar effect in suppressing the observed connectivity estimates also for these other metrics.

We also restricted our investigation to a limited number of configurations of inverse models and connectivity metrics. The rationale beyond these choices was to select the most widely used methods, thus making our results of more general interest. Discussing the difference with respect to all other possible choices is beyond the scope of this work. For instance, we used as source model, both for data generation and for the inverse solution, cortically constrained sources with fixed orientation orthogonal to the local cortical surface. This is a common choice for various source reconstruction techniques (e.g., Dale and Sereno, 1993; Gross et al., 2013; Henson et al., 2009; Hillebrand and Barnes, 2003; Lin et al., 2006; Liu et al., 1998), and it is based on the observation that MEG signals are mostly due post-synaptic currents of pyramidal cells that are perpendicular to the cortical surface (Okada, 1982; Okada et al., 1997). This choice was also driven by the fact that fixing source orientation would reduce the dimensionality of the lead field matrix by a factor 3, with a consequent gain on the number of unknowns to be determined by the solution of the inverse problem.

Our simulations are also limited by the fact that we did not exhaustively study possible effects due to source size and configuration. Here, we simulated signal generators as focal, i.e., point-like, sources which represent the activity of about 7.2 mm^2 given the average spatial density of the cortical mesh. As discussed above, this choice is more advantageous for beamforming than for MNE (see also Hincapié et al., 2017). Hence, it would be interesting to investigate in a future study how our results would change if extended cortical sources were modeled. Furthermore, in our simulated scenario, only two sources were interacting, and we assumed a time-delayed unidirectional source coupling model (Fries, 2015), thus avoiding the issue of zero-time-delay correlation on beamforming source reconstruction (Quraan and Cheyne, 2010; Sekihara et al., 2005; van Veen et al., 1997). More complex interaction scenarios could be investigated in future studies, e.g., with network-like topographies comprising more than two interacting sources.

Overall, the results of the present study provide evidence for how an improved co-registration impacts MEG connectivity analysis. We also discussed the theoretical and practical implications in the use of accurate head models and source reconstruction techniques. Of course, these results are limited by the extent in which our simulations match real-life circumstances. Nonetheless, there is clear evidence that, by reducing co-registration errors, the accuracy of connectivity estimates can significantly improve. Hence, we believe that novel and upcoming technological advances, such as the development of hybrid MEG–ULF MRI systems, which hold promise for more accurate co-registration, will enable effective use of highly accurate head models and will be beneficial for reliable MEG connectivity analysis.

Declarations of interest

None.

Acknowledgements

This work was funded by the European Commission Horizon 2020 research and innovation program under Grant Agreement No. 686865 (BREAKBEN—H2020-FETOPEN-2014-2015/H2020-FETOPEN-2014-2015-RIA). The content reflects only the author's view and the European Commission is not responsible for the content. This work was partially supported by the University of Chieti-Pescara Faculty Resources Grant 2018 of author LM, titled “Development and applications of methods for the study of brain connectivity with Magnetoencephalography and Electroencephalography”. This work was conducted under the framework of the “Departments of Excellence 2018-2022” initiative of the Italian Ministry of Education, University and Research for the Department of Neuroscience, Imaging and Clinical Sciences (DNISC) of the University of Chieti-Pescara.

Appendix A. Supplementary data

Supplementary data to this article can be found online at https://doi.org/10.1016/j.neuroimage.2019.04.061.

References

Adjamian, P., Barnes, G.R., Hillebrand, A., Holliday, I.E., Singh, K.D., Furlong, P.L., Harrington, E., Barclay, C.W., Route, P.J.G., 2004. Co-registration of magnetoencephalography with magnetic resonance imaging using bite-bar-based fiducials and surface-matching. Clin. Neurophysiol. 115, 691–698. https://doi.org/10.1016/j.clinph.2003.10.023.

Avena-Koenigsberger, A., Misic, B., Sporns, O., 2018. Communication dynamics in complex brain networks. Nat. Rev. Neurosci. 19, 17–33. https://doi.org/10.1038/nrn.2017.149.

Baillet, S., 2017. Magnetoencephalography for brain electrophysiology and imaging. Nat. Neurosci. 20, 327–339. https://doi.org/10.1038/nn.4504.

Barratt, E.L., Francis, S.T., Morris, P.G., Brookes, M.J., 2018. Mapping the topological organisation of beta oscillations in motor cortex using MEG. Neuroimage 181, 831–844. https://doi.org/10.1016/j.neuroimage.2018.06.041.

Basti, A., Pizzella, V., Chella, F., Romani, G.L., Nolte, G., Marzetti, L., 2018. Disclosing large-scale directed functional connections in MEG with the multivariate phase slope index. Neuroimage 175, 161–175. https://doi.org/10.1016/j.neuroimage.2018.03.004.

Basti, A., Pizzella, V., Nolte, G., Chella, F., Marzetti, L., 2017. Disclosing brain functional connectivity from electrophysiological signals with phase slope based metrics. J. Serbian Soc. Comput. Mech. 11, 50–62. https://doi.org/10.24874/jsscm.2017.11.02.05.

Bastos, A.M., Schoffelen, J.-M., 2016. A tutorial review of functional connectivity analysis methods and their interpretational pitfalls. Front. Syst. Neurosci. 9. https://doi.org/10.3389/fnsys.2015.00175.

Benjamini, Y., Yekutieli, D., 2001. The control of the false discovery rate in multiple testing under dependency. Ann. Stat. 29, 1165–1188.

Boto, E., Bowtell, R., Krüger, P., Fromhold, T.M., Morris, P.G., Meyer, S.S., Barnes, G.R., Brookes, M.J., 2016. On the potential of a new generation of magnetometers for MEG: a beamformer simulation study. PLoS One 11, e0157655. https://doi.org/10.1371/journal.pone.0157655.

Brookes, M.J., Hale, J.R., Zumer, J.M., Stevenson, C.M., Francis, S.T., Barnes, G.R., Owen, J.P., Morris, P.G., Nagarajan, S.S., 2011a. Measuring functional connectivity using MEG: methodology and comparison with fcMRI. Neuroimage 56, 1082–1104. https://doi.org/10.1016/j.neuroimage.2011.02.054.

Brookes, M.J., Vrba, J., Robinson, S.E., Stevenson, C.M., Peters, A.M., Barnes, G.R., Hillebrand, A., Morris, P.G., 2008. Optimising experimental design for MEG beamformer imaging. Neuroimage 39, 1788–1802. https://doi.org/10.1016/j.neuroimage.2007.09.050.

Brookes, M.J., Woolrich, M., Luckhoo, H., Price, D., Hale, J.R., Stephenson, M.C., Barnes, G.R., Smith, S.M., Morris, P.G., 2011b. Investigating the electrophysiological basis of resting state networks using magnetoencephalography. Proc. Natl. Acad. Sci. 108, 16783–16788. https://doi.org/10.1073/pnas.1112685108.

Brookes, M.J., Woolrich, M.W., Barnes, G.R., 2012. Measuring functional connectivity in MEG: a multivariate approach insensitive to linear source leakage. Neuroimage 63, 910–920. https://doi.org/10.1016/j.neuroimage.2012.03.048.

Chella, F., Marzetti, L., Pizzella, V., Zappasodi, F., Nolte, G., 2014. Third order spectral analysis robust to mixing artifacts for mapping cross-frequency interactions in EEG/MEG. Neuroimage 91, 146–161. https://doi.org/10.1016/j.neuroimage.2013.12.064.

Chella, F., Pizzella, V., Zappasodi, F., Nolte, G., Marzetti, L., 2016. Bispectral pairwise interacting source analysis for identifying systems of cross-frequency interacting brain sources from electroencephalographic or magnetoencephalographic signals. Phys. Rev. E 93, 052420. https://doi.org/10.1103/PhysRevE.93.052420.

Cho, J.-H., Vorwerk, J., Wolters, C.H., Knösche, T.R., 2015. Influence of the head model on EEG and MEG source connectivity analyses. Neuroimage 110, 60–77. https://doi.org/10.1016/j.neuroimage.2015.01.043.

Cohen, J., 1988. Statistical Power Analysis for the Behavioral Sciences, second ed. Erlbaum Associates, Hillsdale.

Colclough, G.L., Woolrich, M.W., Tewarie, P.K., Brookes, M.J., Quinn, A.J., Smith, S.M., 2016. How reliable are MEG resting-state connectivity metrics? Neuroimage 138, 284–293. https://doi.org/10.1016/j.neuroimage.2016.05.070.

Cole, M.W., Bassett, D.S., Power, J.D., Braver, T.S., Petersen, S.E., 2014. Intrinsic and task-evoked network architectures of the human brain. Neuron 83, 238–251. https://doi.org/10.1016/j.neuron.2014.05.014.

Dale, A.M., Fischl, B., Sereno, M.I., 1999. Cortical surface-based analysis: I. Segmentation and surface reconstruction. Neuroimage 9, 179–194. https://doi.org/10.1006/nimg.1998.0395.

Dale, A.M., Sereno, M.I., 1993. Improved localizadon of cortical activity by combining EEG and MEG with MRI cortical surface reconstruction: a linear approach. J. Cogn. Neurosci. 5, 162–176. https://doi.org/10.1162/jocn.1993.5.2.162.

D'Andrea, A., Chella, F., Marshall, T.R., Pizzella, V., Romani, G.L., Jensen, O., Marzetti, L., 2019. Alpha and alpha-beta phase synchronization mediate the recruitment of the visuospatial attention network through the Superior Longitudinal Fasciculus. NeuroImage 188, 722–732. https://doi.org/10.1016/j.neuroimage.2018.12.056.

Darvas, F., Ojemann, J.G., Sorensen, L.B., 2009. Bi-phase locking - a tool for probing non-linear interaction in the human brain. Neuroimage 46, 123–132. https://doi.org/10.1016/j.neuroimage.2009.01.034.

de Munck, J.C., 1992. A linear discretization of the volume conductor boundary integral equation using analytically integrated elements (electrophysiology application). IEEE Trans. Biomed. Eng. 39, 986–990. https://doi.org/10.1109/10.256433.

de Pasquale, F., Della Penna, S., Snyder, A.Z., Lewis, C., Mantini, D., Marzetti, L., Belardinelli, P., Ciancetta, L., Pizzella, V., Romani, G.L., Corbetta, M., 2010. Temporal dynamics of spontaneous MEG activity in brain networks. Proc. Natl. Acad. Sci. 107, 6040. https://doi.org/10.1073/pnas.0913863107.

Engel, A.K., Gerloff, C., Hilgetag, C.C., Nolte, G., 2013. Intrinsic coupling modes: multiscale interactions in ongoing brain activity. Neuron 80, 867–886. https://doi.org/10.1016/j.neuron.2013.09.038.

Ewald, A., Marzetti, L., Zappasodi, F., Meinecke, F.C., Nolte, G., 2012. Estimating true brain connectivity from EEG/MEG data invariant to linear and static transformations in sensor space. Neuroimage 60, 476–488. https://doi.org/10.1016/j.neuroimage.2011.11.084.

Fang, Q., Boas, D.A., 2009. Tetrahedral mesh generation from volumetric binary and grayscale images. In: 2009 IEEE International Symposium on Biomedical Imaging: from Nano to Macro. Presented at the 2009 IEEE International Symposium on Biomedical Imaging: from Nano to Macro, pp. 1142–1145. https://doi.org/10.1109/ISBI.2009.5193259.

Fischl, B., 2012. FreeSurfer. NeuroImage, 20 YEARS of fMRI 62, pp. 774–781. https://doi.org/10.1016/j.neuroimage.2012.01.021.

Fischl, B., Sereno, M.I., Dale, A.M., 1999. Cortical surface-based analysis: II: inflation, flattening, and a surface-based coordinate system. Neuroimage 9, 195–207. https://doi.org/10.1006/nimg.1998.0396.

Fries, P., 2015. Rhythms for cognition: communication through coherence. Neuron 88, 220–235. https://doi.org/10.1016/j.neuron.2015.09.034.

Fritz, C.O., Morris, P.E., Richler, J.J., 2012. Effect size estimates: current use, calculations, and interpretation. J. Exp. Psychol. Gen. 141, 2–18. https://doi.org/10.1037/a0024338.

Geweke, J., 1982. Measurement of linear dependence and feedback between multiple time series. J. Am. Stat. Assoc. 77, 304–313. https://doi.org/10.2307/2287238.

Gross, J., Baillet, S., Barnes, G.R., Henson, R.N., Hillebrand, A., Jensen, O., Jerbi, K., Litvak, V., Maess, B., Oostenveld, R., Parkkonen, L., Taylor, J.R., van Wassenhove, V., Wibral, M., Schoffelen, J.-M., 2013. Good practice for conducting and reporting MEG research. Neuroimage 65, 349–363. https://doi.org/10.1016/j.neuroimage.2012.10.001.

Guidotti, R., Sinibaldi, R., Luca, C.D., Conti, A., Ilmoniemi, R.J., Zevenhoven, K.C.J., Magnelind, P.E., Pizzella, V., Gratta, C.D., Romani, G.L., Penna, S.D., 2018. Optimized 3D co-registration of ultra-low-field and high-field magnetic resonance images. PLoS One 13, e0193890. https://doi.org/10.1371/journal.pone.0193890.

Hämäläinen, M., Hari, R., Ilmoniemi, R.J., Knuutila, J., Lounasmaa, O.V., 1993. Magnetoencephalography—theory, instrumentation, and applications to noninvasive studies of the working human brain. Rev. Mod. Phys. 65, 413–497. https://doi.org/10.1103/RevModPhys.65.413.

Hämäläinen, M.S., Ilmoniemi, R.J., 1994. Interpreting magnetic fields of the brain: minimum norm estimates. Med. Biol. Eng. Comput. 32, 35–42. https://doi.org/10.1007/BF02512476.

Hämäläinen, M.S., Sarvas, J., 1989. Realistic conductivity geometry model of the human head for interpretation of neuromagnetic data. IEEE Trans. Biomed. Eng. 36, 165–171. https://doi.org/10.1109/10.16463.

Haueisen, J., Ramon, C., Eiselt, M., Brauer, H., Nowak, H., 1997. Influence of tissue resistivities on neuromagnetic fields and electric potentials studied with a finite element model of the head. IEEE Trans. Biomed. Eng. 44, 727–735. https://doi.org/10.1109/10.605429.

Haufe, S., Ewald, A., 2016. A simulation framework for benchmarking EEG-based brain connectivity estimation methodologies. Brain Topogr. 1–18. https://doi.org/10.1007/s10548-016-0498-y.

Haufe, S., Nikulin, V.V., Müller, K.-R., Nolte, G., 2013. A critical assessment of connectivity measures for EEG data: a simulation study. Neuroimage 64, 120–133. https://doi.org/10.1016/j.neuroimage.2012.09.036.

Hauk, O., Stenroos, M., 2014. A framework for the design of flexible cross-talk functions for spatial filtering of EEG/MEG data: DeFleCT. Hum. Brain Mapp. 35, 1642–1653. https://doi.org/10.1002/hbm.22279.

Henson, R.N., Mattout, J., Phillips, C., Friston, K.J., 2009. Selecting forward models for MEG source-reconstruction using model-evidence. Neuroimage 46, 168–176. https://doi.org/10.1016/j.neuroimage.2009.01.062.

Hillebrand, A., Barnes, G.R., 2011. Practical constraints on estimation of source extent with MEG beamformers. Neuroimage 54, 2732–2740. https://doi.org/10.1016/j.neuroimage.2010.10.036.

Hillebrand, A., Barnes, G.R., 2003. The use of anatomical constraints with MEG beamformers. Neuroimage 20, 2302–2313. https://doi.org/10.1016/j.neuroimage.2003.07.031.

Hincapié, A.-S., Kujala, J., Mattout, J., Pascarella, A., Daligault, S., Delpuech, C., Mery, D., Cosmelli, D., Jerbi, K., 2017. The impact of MEG source reconstruction method on source-space connectivity estimation: a comparison between minimum-norm solution and beamforming. Neuroimage 156, 29–42. https://doi.org/10.1016/j.neuroimage.2017.04.038.

Hipp, J.F., Hawellek, D.J., Corbetta, M., Siegel, M., Engel, A.K., 2012. Large-scale cortical correlation structure of spontaneous oscillatory activity. Nat. Neurosci. 15, 884–890.

Iivanainen, J., Stenroos, M., Parkkonen, L., 2017. Measuring MEG closer to the brain: performance of on-scalp sensor arrays. Neuroimage 147, 542–553. https://doi.org/10.1016/j.neuroimage.2016.12.048.

Jenkinson, M., Beckmann, C.F., Behrens, T.E.J., Woolrich, M.W., Smith, S.M., 2012. FSL. NeuroImage, 20 YEARS of fMRI 62, pp. 782–790. https://doi.org/10.1016/j.neuroimage.2011.09.015.

Kaipio, J., Somersalo, E., 2007. Statistical inverse problems: discretization, model reduction and inverse crimes. J. Comput. Appl. Math., Special Issue: Applied Computational Inverse Problems 198, 493–504. https://doi.org/10.1016/j.cam.2005.09.027.

Lachaux, J.-P., Rodriguez, E., Martinerie, J., Varela, F.J., 1999. Measuring phase synchrony in brain signals. Hum. Brain Mapp. 8, 194–208. <194::AID-HBM4>3.0.CO;2-C. https://doi.org/10.1002/(SICI)1097-0193(1999)8:4.

Lew, S., Wolters, C.H., Dierkes, T., Röer, C., MacLeod, R.S., 2009. Accuracy and run-time comparison for different potential approaches and iterative solvers in finite element method based EEG source analysis. Appl. Numer. Math. 59. https://doi.org/10.1016/j.apnum.2009.02.006, 1970–1988.

Lin, F.-H., Witzel, T., Ahlfors, S.P., Stufflebeam, S.M., Belliveau, J.W., Hämäläinen, M.S., 2006. Assessing and improving the spatial accuracy in MEG source localization by depth-weighted minimum-norm estimates. Neuroimage 31, 160–171. https://doi.org/10.1016/j.neuroimage.2005.11.054.

Lin, F.-H., Witzel, T., Hämäläinen, M.S., Dale, A.M., Belliveau, J.W., Stufflebeam, S.M., 2004. Spectral spatiotemporal imaging of cortical oscillations and interactions in the human brain. Neuroimage 23, 582–595. https://doi.org/10.1016/j.neuroimage.2004.04.027.

Liu, A.K., Belliveau, J.W., Dale, A.M., 1998. Spatiotemporal imaging of human brain activity using functional MRI constrained magnetoencephalography data: Monte Carlo simulations. Proc. Natl. Acad. Sci. 95, 8945.

Liu, Q., Farahibozorg, S., Porcaro, C., Wenderoth, N., Mantini, D., 2017. Detecting large-scale networks in the human brain using high-density electroencephalography. Hum. Brain Mapp. 38, 4631–4643. https://doi.org/10.1002/hbm.23688.

Liuzzi, L., Gascoyne, L.E., Tewarie, P.K., Barratt, E.L., Boto, E., Brookes, M.J., 2017. Optimising experimental design for MEG resting state functional connectivity measurement. Neuroimage 155, 565–576. https://doi.org/10.1016/j.neuroimage.2016.11.064.

Lobier, M., Palva, J.M., Palva, S., 2018. High-alpha band synchronization across frontal, parietal and visual cortex mediates behavioral and neuronal effects of visuospatial attention. Neuroimage 165, 222–237. https://doi.org/10.1016/j.neuroimage.2017.10.044.

López, J.D., Penny, W.D., Espinosa, J.J., Barnes, G.R., 2012. A general Bayesian treatment for MEG source reconstruction incorporating lead field uncertainty. Neuroimage 60, 1194–1204. https://doi.org/10.1016/j.neuroimage.2012.01.077.

Lütkepohl, H., 2005. New Introduction to Multiple Time Series Analysis. Springer-Verlag, Berlin Heidelberg.

Mäkelä, N., Stenroos, M., Sarvas, J., Ilmoniemi, R.J., 2018. Truncated RAP-MUSIC (TRAP-MUSIC) for MEG and EEG source localization. Neuroimage 167, 73–83. https://doi.org/10.1016/j.neuroimage.2017.11.013.

Mäkinen, A.J., Zevenhoven, K.C.J., Ilmoniemi, R.J., 2019. Automatic spatial calibration of Ultra-Low-Field MRI for High-Accuracy Hybrid MEG–MRI. IEEE Trans. Med. Imaging. https://doi.org/10.1109/TMI.2019.2905934.

Marzetti, L., Penna, S.D., Snyder, A.Z., Pizzella, V., Nolte, G., Pasquale, F. de, Romani, G.L., Corbetta, M., 2013. Frequency specific interactions of MEG resting state activity within and across brain networks as revealed by the multivariate interaction measure. Neuroimage 79, 172–183. https://doi.org/10.1016/j.neuroimage.2013.04.062.

Mosher, J.C., Leahy, R.M., 1999. Source localization using recursively applied and projected (RAP) MUSIC. IEEE Trans. Signal Process. 47, 332–340. https://doi.org/10.1109/78.740118.

Mosher, J.C., Leahy, R.M., 1998. Recursive MUSIC: a framework for EEG and MEG source localization. IEEE Trans. Biomed. Eng. 45, 1342–1354. https://doi.org/10.1109/10.725331.

Mosher, J.C., Leahy, R.M., Lewis, P.S., 1999. EEG and MEG: forward solutions for inverse methods. IEEE Trans. Biomed. Eng. 46, 245–259. https://doi.org/10.1109/10.748978.

Neugebauer, F., Möddel, G., Rampp, S., Burger, M., Wolters, C.H., 2017. The effect of head model simplification on beamformer source localization. Front. Neurosci. 11, 625. https://doi.org/10.3389/fnins.2017.00625.

Nolte, G., Bai, O., Wheaton, L., Mari, Z., Vorbach, S., Hallett, M., 2004. Identifying true brain interaction from EEG data using the imaginary part of coherency. Clin. Neurophysiol. 115, 2292–2307. https://doi.org/10.1016/j.clinph.2004.04.029.

Nolte, G., Ziehe, A., Nikulin, V.V., Schlögl, A., Krämer, N., Brismar, T., Müller, K.-R., 2008. Robustly estimating the flow direction of information in complex physical systems. Phys. Rev. Lett. 100, 234101. https://doi.org/10.1103/PhysRevLett.100.234101.

Okada, Y., 1982. Neurogenesis of evoked magnetic fields. Biomagnetism: an Interdiciplinary Approach. Pergamon Press, New York, NY.

Okada, Y.C., Wu, J., Kyuhou, S., 1997. Genesis of MEG signals in a mammalian CNS structure. Electroencephalogr. Clin. Neurophysiol. 103, 474–485. https://doi.org/10.1016/S0013-4694(97)00043-6.

O'Neill, G.C., Barratt, E.L., Hunt, B.A.E., Tewarie, P.K., Brookes, M.J., 2015. Measuring electrophysiological connectivity by power envelope correlation: a technical review on MEG methods. Phys. Med. Biol. 60, R271. https://doi.org/10.1088/0031-9155/60/21/R271.

Özkurt, T.E., 2016. Estimation of nonlinear neural source interactions via sliced bicoherence. Biomed. Signal Process. Control 30, 43–52. https://doi.org/10.1016/j.bspc.2016.05.001.

Palva, J.M., Wang, S.H., Palva, S., Zhigalov, A., Monto, S., Brookes, M.J., Schoffelen, J.-M., Jerbi, K., 2018. Ghost interactions in MEG/EEG source space: a note of caution on inter-areal coupling measures. Neuroimage 173, 632–643. https://doi.org/10.1016/j.neuroimage.2018.02.032.

Palva, S., Palva, J.M., 2012. Discovering oscillatory interaction networks with M/EEG: challenges and breakthroughs. Trends Cognit. Sci. 16, 219–230. https://doi.org/10.1016/j.tics.2012.02.004.

Pereda, E., Quiroga, R.Q., Bhattacharya, J., 2005. Nonlinear multivariate analysis of neurophysiological signals. Prog. Neurobiol. 77, 1–37. https://doi.org/10.1016/j.pneurobio.2005.10.003.

Quraan, M.A., Cheyne, D., 2010. Reconstruction of correlated brain activity with adaptive spatial filters in MEG. Neuroimage 49, 2387–2400. https://doi.org/10.1016/j.neuroimage.2009.10.012.

Raichle, M.E., 2010. Two views of brain function. Trends Cognit. Sci. 14, 180–190. https://doi.org/10.1016/j.tics.2010.01.008.

Schimpf, P.H., Ramon, C., Haueisen, J., 2002. Dipole models for the EEG and MEG. IEEE Trans. Biomed. Eng. 49, 409–418. https://doi.org/10.1109/10.995679.

Schmidt, R., 1986. Multiple emitter location and signal parameter estimation. IEEE Trans. Antennas Propag. 34, 276–280. https://doi.org/10.1109/TAP.1986.1143830.

Sekihara, K., Nagarajan, S.S., 2008. Adaptive Spatial Filters for Electromagnetic Brain Imaging. In: Series in Biomedical Engineering. Springer-Verlag, Berlin Heidelberg.

Sekihara, K., Sahani, M., Nagarajan, S.S., 2005. Localization bias and spatial resolution of adaptive and non-adaptive spatial filters for MEG source reconstruction. Neuroimage 25, 1056–1067. https://doi.org/10.1016/j.neuroimage.2004.11.051.

Siegel, M., Donner, T.H., Oostenveld, R., Fries, P., Engel, A.K., 2008. Neuronal synchronization along the dorsal visual pathway reflects the focus of spatial attention. Neuron 60, 709–719. https://doi.org/10.1016/j.neuron.2008.09.010.

Sommariva, S., Sorrentino, A., Piana, M., Pizzella, V., Marzetti, L., 2017. A comparative study of the robustness of frequency-domain connectivity measures to finite data length. Brain Topogr. 1–21. https://doi.org/10.1007/s10548-017-0609-4.

Sonntag, H., Haueisen, J., Maess, B., 2018. Quality assessment of MEG-to-MRI coregistrations. Phys. Med. Biol. 63, 075003. https://doi.org/10.1088/1361-6560/aab248.

Soto, J.L.P., Lachaux, J.-P., Baillet, S., Jerbi, K., 2016. A multivariate method for estimating cross-frequency neuronal interactions and correcting linear mixing in MEG data, using canonical correlations. J. Neurosci. Methods 271, 169–181. https://doi.org/10.1016/j.jneumeth.2016.07.017.

Stenroos, M., Hunold, A., Haueisen, J., 2014. Comparison of three-shell and simplified volume conductor models in magnetoencephalography. Neuroimage 94, 337–348. https://doi.org/10.1016/j.neuroimage.2014.01.006.

Stenroos, M., Mäntynen, V., Nenonen, J., 2007. A Matlab library for solving quasi-static volume conduction problems using the boundary element method. Comput. Methods Progr. Biomed. 88, 256–263. https://doi.org/10.1016/j.cmpb.2007.09.004.

Stenroos, M., Nummenmaa, A., 2016. Incorporating and compensating cerebrospinal fluid in surface-based forward models of magneto- and electroencephalography. PLoS One 11, e0159595. https://doi.org/10.1371/journal.pone.0159595.

Stenroos, M., Sarvas, J., 2012. Bioelectromagnetic forward problem: isolated source approach revis(it). Phys. Med. Biol. 57, 3517. https://doi.org/10.1088/0031-9155/57/11/3517.

Tass, P., Rosenblum, M.G., Weule, J., Kurths, J., Pikovsky, A., Volkmann, J., Schnitzler, A., Freund, H.-J., 1998. Detection of $\mathit{n}:\mathit{m}$ phase locking from noisy data: application to magnetoencephalography. Phys. Rev. Lett. 81, 3291–3294. https://doi.org/10.1103/PhysRevLett.81.3291.

Taulu, S., Simola, J., 2006. Spatiotemporal signal space separation method for rejecting nearby interference in MEG measurements. Phys. Med. Biol. 51, 1759. https://doi.org/10.1088/0031-9155/51/7/008.

Troebinger, L., López, J.D., Lutti, A., Bradbury, D., Bestmann, S., Barnes, G., 2014. High precision anatomy for MEG. Neuroimage 86, 583–591. https://doi.org/10.1016/j.neuroimage.2013.07.065.

Uutela, K., Taulu, S., Hämäläinen, M., 2001. Detecting and correcting for head movements in neuromagnetic measurements. Neuroimage 14, 1424–1431. https://doi.org/10.1006/nimg.2001.0915.

van Veen, B.D., Drongelen, W.V., Yuchtman, M., Suzuki, A., 1997. Localization of brain electrical activity via linearly constrained minimum variance spatial filtering. IEEE Trans. Biomed. Eng. 44, 867–880. https://doi.org/10.1109/10.623056.

Varela, F., Lachaux, J.-P., Rodriguez, E., Martinerie, J., 2001. The brainweb: phase synchronization and large-scale integration. Nat. Rev. Neurosci. 2, 229–239. https://doi.org/10.1038/35067550.

Vesanen, P.T., Nieminen, J.O., Zevenhoven, K.C.J., Dabek, J., Parkkonen, L.T., Zhdanov, A.V., Luomahaara, J., Hassel, J., Penttilä, J., Simola, J., Ahonen, A.I., Mäkelä, J.P., Ilmoniemi, R.J., 2013. Hybrid ultra-low-field MRI and magnetoencephalography system based on a commercial whole-head neuromagnetometer. Magn. Reson. Med. 69, 1795–1804. https://doi.org/10.1002/mrm.24413.

Vinck, M., Oostenveld, R., Wingerden, M., vanBattaglia, F., Pennartz, C.M.A., 2011. An improved index of phase-synchronization for electrophysiological data in the presence of volume-conduction, noise and sample-size bias. Neuroimage 55, 1548–1565. https://doi.org/10.1016/j.neuroimage.2011.01.055.

Vorwerk, J., Cho, J.-H., Rampp, S., Hamer, H., Knösche, T.R., Wolters, C.H., 2014. A guideline for head volume conductor modeling in EEG and MEG. Neuroimage 100, 590–607. https://doi.org/10.1016/j.neuroimage.2014.06.040.

Wakeman, D.G., Henson, R.N., 2015. A multi-subject, multi-modal human neuroimaging dataset. Sci. Data 2, 150001. https://doi.org/10.1038/sdata.2015.1.

Wehner, D.T., Hämäläinen, M.S., Mody, M., Ahlfors, S.P., 2008. Head movements of children in MEG: quantification, effects on source estimation, and compensation. Neuroimage 40, 541–550. https://doi.org/10.1016/j.neuroimage.2007.12.026.

Whalen, C., Maclin, E.L., Fabiani, M., Gratton, G., 2008. Validation of a method for coregistering scalp recording locations with 3D structural MR images. Hum. Brain Mapp. 29, 1288–1301. https://doi.org/10.1002/hbm.20465.

Windhoff, M., Opitz, A., Thielscher, A., 2013. Electric field calculations in brain stimulation based on finite elements: an optimized processing pipeline for the generation and usage of accurate individual head models. Hum. Brain Mapp. 34, 923–935. https://doi.org/10.1002/hbm.21479.

Wolters, C.H., Anwander, A., Tricoche, X., Weinstein, D., Koch, M.A., MacLeod, R.S., 2006. Influence of tissue conductivity anisotropy on EEG/MEG field and return current computation in a realistic head model: a simulation and visualization study using high-resolution finite element modeling. Neuroimage 30, 813–826. https://doi.org/10.1016/j.neuroimage.2005.10.014.

Wolters, C.H., Grasedyck, L., Hackbusch, W., 2004. Efficient computation of lead field bases and influence matrix for the FEM-based EEG and MEG inverse problem. Inverse Probl. 20, 1099. https://doi.org/10.1088/0266-5611/20/4/007.

Zetter, R., Iivanainen, J., Stenroos, M., Parkkonen, L., 2018. Requirements for coregistration accuracy in on-scalp MEG. Brain Topogr. 1–18. https://doi.org/10.1007/s10548-018-0656-5.

Zotev, V.S., Matlashov, A.N., Volegov, P.L., Savukov, I.M., Espy, M.A., Mosher, J.C., Gomez, J.J., Kraus, R.H., 2008. Microtesla MRI of the human brain combined with MEG. J. Magn. Reson. 194, 115–120. https://doi.org/10.1016/j.jmr.2008.06.007.